SANDIA REPORT

SAND2015-8282
Unlimited Release
Printed September 2015

A Kinetic Approach to Modeling the Manufacture of High Density Polyurethane Structural Foam: Foaming and Polymerization

Rekha Rao, Lisa Mondy, David Noble, Victor Brunini, James Tinsley, Christine Roberts, Kevin Long, Melissa Soehnel, Mathew Celina, Nicholas Wyatt, Kyle Thompson

Prepared by
Sandia National Laboratories
Albuquerque, New Mexico 87185 and Livermore, California 94550

Sandia National Laboratories is a multi-program laboratory managed and operated by Sandia Corporation, a wholly owned subsidiary of Lockheed Martin Corporation, for the U.S. Department of Energy's National Nuclear Security Administration under contract DE-AC04-94AL85000.

Issued by Sandia National Laboratories, operated for the United States Department of Energy by Sandia Corporation.

Available to DOE and DOE contractors from
U.S. Department of Energy
Office of Scientific and Technical Information
P.O. Box 62
Oak Ridge, TN 37831

Telephone: (865) 576-8401
Facsimile: (865) 576-5728
E-Mail: reports@adonis.osti.gov
Online ordering: http://www.osti.gov/bridge

Available to the public from
U.S. Department of Commerce
National Technical Information Service
5285 Port Royal Rd.
Springfield, VA 22161

Telephone: (800) 553-6847
Facsimile: (703) 605-6900
E-Mail: orders@ntis.fedworld.gov
Online order: http://www.ntis.gov/help/ordermethods.asp?loc=7-4-0#online

SAND2015-8282
Unlimited Release
Printed September 2015

A Kinetic Approach to Polyurethane Foam Structural Modeling

Rekha Rao, Lisa Mondy, David Noble
Fluid Sciences & Engineering

Christine Roberts, Melissa Soehnel
Thermal/Fluid Experimental Sciences

Victor Brunini
Thermal/Fluid Science and Engineering

Kevin Long
Solid Mechanics

Mathew Celina
Materials Characterization & Performance

Kyle Thompson
Radiography & Modal Testing

Sandia National Laboratories
P.O. Box 5800
Albuquerque, New Mexico 87185-MS0836

James Tinsley
Honeywell National Security Campus

Abstract

This report details the study of PMDI structural foam and the development of a computational model to represent it. This polyurethane has a fast catalyst, such that foaming and polymerization occur simultaneously. The foam is over-packed to twice or more of its free rise density to reach the density of interest. Our approach is to combine model development closely with experiments to discover underlying physical phenomena, to parameterize models, and to validate the models once they have been developed. The model must be able to represent the expansion, filling of molds, curing, and final foam properties. PMDI is a chemically blown foam, where carbon dioxide is produced via the reaction of water and isocyanate. The isocyanate also reacts with polyol in a competing reaction, which produces the polymer. A new kinetic model is developed and implemented, which follows a simplified mathematical formalism that decouples these two reactions. The model predicts the polymerization reaction via condensation chemistry, where vitrification and glass transition temperature evolution must be included to correctly predict the temperature dependence of the kinetics. The foam gas generation kinetics are determined by tracking the molar concentration of both water and carbon dioxide. Understanding the thermal history and loads on the foam due to exothermicity and oven curing is very important to the results, since the kinetics and material properties are all sensitive to temperature. The

conservation equations, including the equations of motion, an energy balance, and three rate equations are solved via a stabilized finite element method. We assume generalized-Newtonian rheology that is dependent on the extent of cure, gas fraction, and temperature. The conservation equations are combined with a level set method to determine the location of the free surface over time. Results from the model are compared to experimental flow visualization data and post-test X-ray computed tomography (CT) data for the density. Several geometries are investigated including a mock encapsulation part, two configurations of a mock structural part, and a bar geometry to specifically test the density model. We have found that the model predicts both average density and filling profiles well. However, it under predicts density gradients, especially in the gravity direction. Further model improvements are also discussed.

Acknowledgments

The authors would like to acknowledge helpful discussions with Shayna Begay, Kyle Zufelt, (2153), and personnel at National Nuclear Security Administration's National Security Campus, Operated by Honeywell Federal Manufacturing & Technologies, LLC, including James Mahoney, Angela Kartsonis, Audrey Chase, and Vinita Chhahira. I would like to thank my reviewers, Kevin Troyer and Jeremy Lechman, for their timely and insightful comments. Funding for this project came from ASC PE&M, WSEAT, and the B61 program. We are grateful for their support.

Contents

Figures

Tables

Nomenclature

a_T	time shift factor
ATR	attenuated total reflection
C_p	heat capacity per unit mass
CO_2	carbon dioxide
DSC	differential scanning calorimeter
E	activation energy
$\boldsymbol{g}$	gravity constant
ΔH_{rxn}	heat of reaction
k	thermal conductivity
NSC	National Nuclear Security Administration's National Security Campus, Operated by Honeywell Federal Manufacturing & Technologies, LLC
IR	infrared
n	number of moles
p	pressure
R	universal gas constant
R-component	resin part of the foam kit
PMDI	polyurethane foam based on polymethylene diisocyanate
SEM	scanning electron microscopy
t	time
T	absolute temperature
T-component	curative part of the foam kit
v	mass averaged velocity
V	volume
Y	liquid mass fraction
κ	foam bulk viscosity
η	foam (apparent Newtonian) viscosity
ξ	extent of polymerization reaction
ρ	density of the foam
$\underline{\underline{\boldsymbol{\tau}}}$	fluid stress tensor
ϕ	gas fraction
ω	angular frequency

1. INTRODUCTION

Foams are multiphase materials with a compressible gas dispersed as bubbles in a continuous phase. Here we are interested in understanding the manufacturing of chemically blown polymeric foams, which evolve from low viscosity Newtonian liquids to bubbly liquids via gas generation, finally producing solid foam through polymerization. In these foams, bubble microstructure can affect macroscopic properties such as material strength and density. Bubble-scale effects such as liquid drainage, coarsening, coalescence and rupture can play a significant role in foam material properties, implying that a multiscale approach may be necessary to produce a truly high-fidelity model.

Characterizing foam can be very difficult since foams are opaque and microstructure. The process of making experimental measurements can alter foam. For instance, the microstructure can evolve in reversible and irreversible manners. If you shear foams, bubbles will move away from the high shear regions; however, above a critical shear rate, bubbles will not have time to react and will rupture instead. Thus, measuring viscosity is fraught with technical challenges. The evolving volume is an additional challenge as we seek to understand this complex, time-dependent material. Models are needed to reduce defects such as voids, out-of-specification density, density gradients, foam decomposition from high temperatures due to exotherms, and incomplete filling. Models are also needed to optimize processing parameters such as vent and gate location, oven temperatures, mold orientation, and filling rates.

We are developing computational models to elucidate the expansion and dynamic filling process of moderately high density polyurethane structural foam, polymeric methylene diphenyl diisocyanate (BKC 44306 PMDI-10). Here the "10" indicates the density of the free rise foam will be roughly 10 lb/ft^3, though it is often over-packed to twice (or more) of its free rise density to reach the density of interest. This polyurethane has a fast catalyst, such that filling and polymerization occur simultaneously. Our approach is to combine model development closely with experiments to better understand foaming phenomena, to parameterize models, and to validate the models once they have been developed. The model must be able to represent the expansion, filling, curing, and final foam properties, all of which is quite challenging. The model is also being used to provide initial conditions for structural mechanics predictions of manufacturing and aging deformations [Long et al., 2015]

The polyurethane of interest is a chemically blown foam, where carbon dioxide is produced via the reaction of water, the blowing agent, and isocyanate. The isocyanate also reacts with polyol in a competing reaction, which produces the polymer. Examples of a free rise sample of PMDI and a molded part are shown in Figure 1.

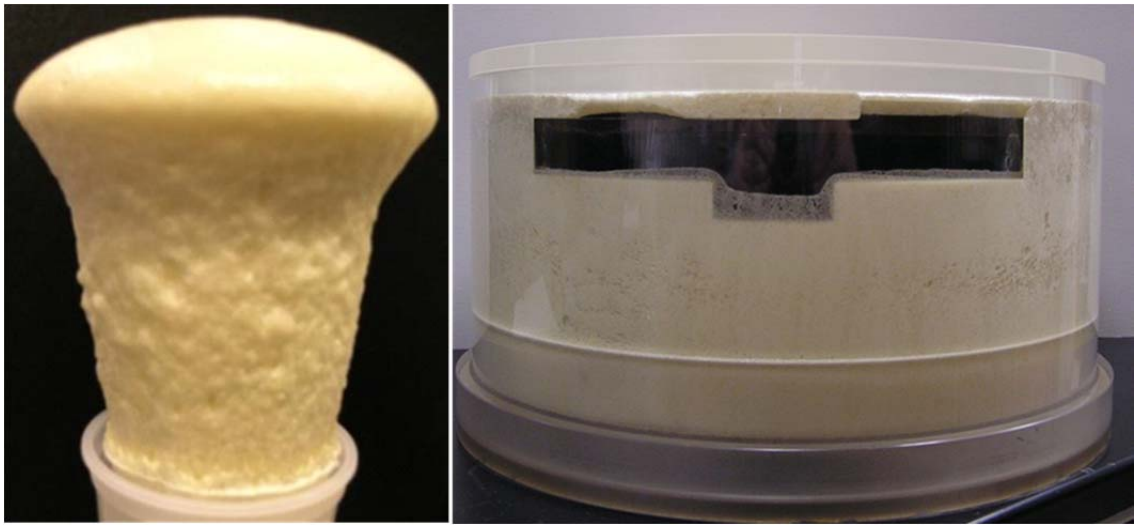

Figure 1. PMDI has a short pot-life: models can help reduce defects and improve filling process. The picture on the left is a free rise foam and the one on the right is idealized structural foam part.

Polyurethane foaming and curing has been studied by a number of researchers. Baser and Khakhar developed kinetic equations and a one-dimensional model to elucidate foam expansion over time for a water and R-11 blown foam, by assuming first order reaction kinetics for the blowing reaction [Baser and Kharkhar, 1994]. Lefebre and Keunings developed a finite element model of reaction polymeric foam extrusion using proprietary kinetics that they do not discuss in detail [Lefebre and Keunings, 1995]. Haberstroh and Zabold use the commercial software CFX with a residence time approach to density predictions to understand free rise foams in two-dimensions [Haberstroh and Zabold, 2004]. Seo et al. used a time-dependent density function fit to data to model foam expansion using a finite volume method [Seo et al., 2003]. They later extended this work to use Baser and Kharkhar kinetics for the foaming reaction and predicting three-dimensional foam expansion to produce a refrigerator cavity [Seo and Youn, 2005]. They used a Castro-Mascosko curing viscosity model with a correction for gas bubbles based on a dilute assumption. Mao et al. used an Eulerian flux-splitting method to integrate the equations of motion and Baser and Khakhar kinetics, with a constant viscosity. They include a prediction of bubble-radius based on the gas volume fraction and an estimate of bubble number density. From this, they predict the filling behavior of a free rise foam, a Hele-Shaw flow and complex three-dimensional geometry [Mao et al., 2005]. Their model predicts local density using an influence volume approach, but is not compared to experimental results. The work is quite impressive though poorly cited, possibly because it is a difficult–to-obtain conference proceeding. Geier et al. also use Baser and Kharkhar kinetics but fit the experimental parameters to thermal experimental data for both foaming and curing [Geier et al., 2009]. They have implemented their model using a finite volume discretization in the commercial code Fluent, where the front between the foam and gas is tracked with a volume of fluid equation. They show comparisons to experiment for front shape and temperature for a free-rise foam and also use the model for filling a refrigerator cavity. Bikard et al. have developed a three-dimension space-time finite element method with reduced order foaming kinetics that they implemented directly in the continuity equation [Bikard et al., 2007]. They use a Piloyan law for the curing reaction and Castro-Macosko curing rheology, including bubble-effects on the rheology using bubble-scale modeling

from Bikard et al. [Bikard et al., 2005]. They model a simple geometry of free-rise foam to critically appraise the modeling results and also provide an industrial example, production of a car seat.

Rao and coworkers developed an engineering model combining the equations of motion, an energy balance, a density model to represent the foam blowing reaction, and a rate equation for the polymerization reaction for polyurethane PMDI-4 encapsulation foam [Rao et al. 2010] and an epoxy foam with a Fluorinert^{TM} physical blowing agent called EFAR foam [Rao et al., 2011]. The material models for these foams were combined with a level set method to track the location of the free surface as it evolves in time. The equations describing the kinetics of the polymerization reaction were of the form of condensation chemistry and were populated through micro-attenuated total reflection (ATR) infrared (IR) spectroscopy measurements. Unfortunately, no IR peak is a fingerprint of the gas-forming reaction. Therefore, the blowing reaction effects were approximated through an empirical, temperature-dependent, equation for the density as a function of time, following Seo et al. [2003]. However, this approach leads to prediction of a constant density throughout the foam at any one time. Unfortunately, to really understand the foaming process, we need to be able to predict both density evolution and local density behavior, which might lead to gradients and affect the final foam strength and structural response [Long et al., 2015]. For this reason, we have been working on a detailed kinetic model of the foaming reaction.

Our approach is unique though it builds on the previous literature and our previous modeling work. We have developed a new kinetic model, which follows a simplified mathematical formalism that decouples foaming and curing reactions. This approach is thoroughly grounded in experimental data, where we have seen that the isocyanate is always in excess and does not affect the kinetics [Mondy et al., 2014]. The model predicts the polymerization reaction via condensation chemistry, where vitrification and glass transition temperature evolution must be included to correctly predict the temperature-dependence of the kinetics. The foam gas generation kinetics are determined by tracking the molar concentration of both water and carbon dioxide using a volume tracking experiment to fit the reaction. Understanding the thermal history and loads on the foam due to exothermicity and oven heating is very important to the results, since the kinetics and material properties are all very sensitive to temperature. The conservation equations, including the equations of motion, an energy balance, and three rate equations are solved via a stabilized finite element method. We assume generalized-Newtonian rheology that is dependent on the cure, gas fraction, and temperature. The conservation equations are combined with a level set method to determine the location of the free surface over time.

In this paper, we focus on the details of a computational model that predicts the density of the foam as it evolves. The details of the experiments used to inform and populate the model are available in a companion report [Mondy et al., 2014]. The paper is organized in the following manner. In the first section we discuss the equations of motion and constitutive equations for the foam chemo-rheology. In the next section, we briefly describe the numerical methods, but mostly reference our previous papers and reports. The third section will briefly discuss measurements for the reactions rates and rheology, include details of how we fit the data and the resulting parameterizations. Thermal properties are summarized for input to the energy equation including the heat of reaction, heat capacity, and thermal conductivity, and their dependence on the foam

density. The final density of foam blown in a simple channel, under both free-rise and over-packed conditions is discussed and later used to evaluate the efficacy of the model.

Results from the model are compared to experimental flow visualization data and post-test CT data for the density. Several geometries are investigated including a mock encapsulation part, two configurations of a mock structural part, and a bar geometry to specifically test the density model. We have found that the model predicts both average density and filling profiles well. However, it under predicts density gradients, especially in the gravity direction. Thoughts on model improvements are also discussed. We conclude with our thoughts on the model and our plans for future work.

2. CONTINUUM MODEL FOR POLYURETHANE FOAM

Polyurethanes are chemically blown foams that begin as two-part mixtures, with polyisocyanate in one part (the curative or T-component) and polyol, water, surfactant and catalyst in the other part (the resin or R-component). When mixed together, several competing reactions occur simultaneously, the most important of which are the polymerization reaction and the foaming reaction (Figure 2). Polymerization occurs via a condensation reaction of polyisocyanate and polyol to form a crosslinked polyurethane. The foaming reaction occurs between polyisocyanate and water, forming carbamic acid which then decomposes to form carbon dioxide (CO_2) and an amine group [Tesser 2004]. The carbon dioxide is a gas, which is responsible for blowing the polymer into a foam. Several secondary reactions occur, when products of the primary reactions react with isocyanate to produce polyurea, biuret, and allophanate.

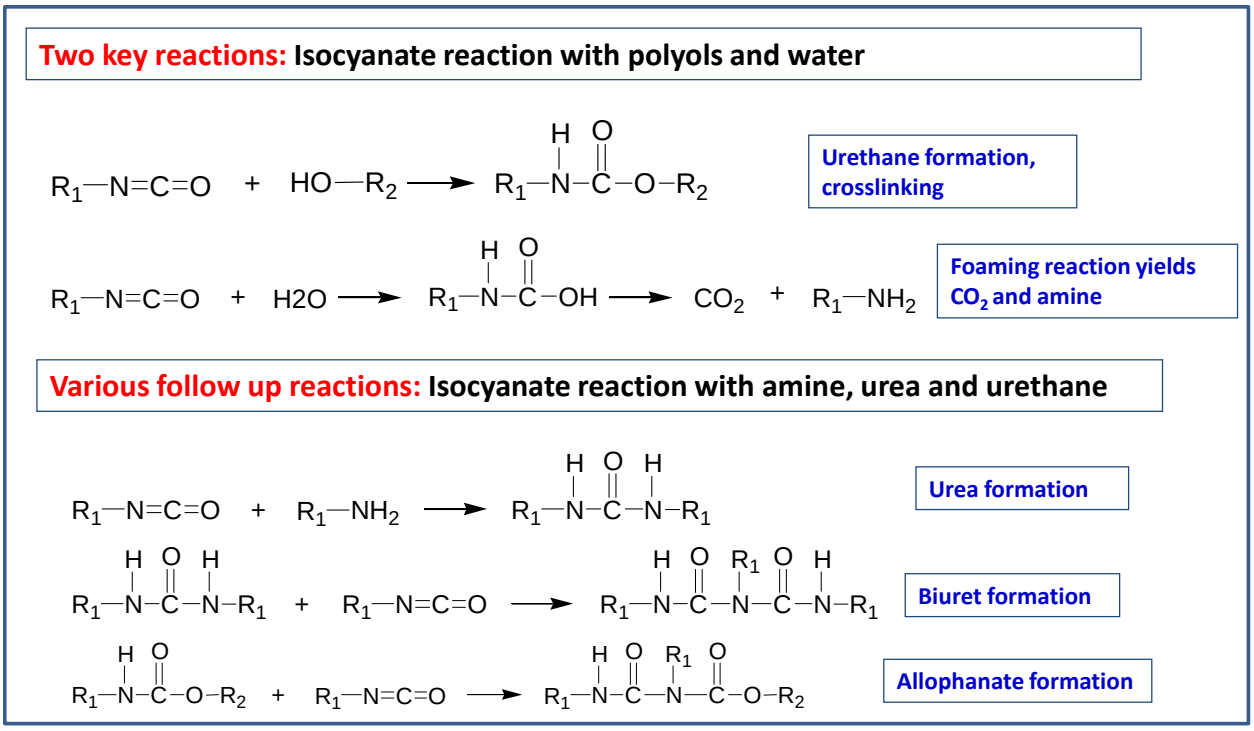

Figure 2. The two primary chemical reactions and three secondary reactions involved in producing solid polyurethane foam.

To help elucidate the expansion and curing of polyurethane foam, we have developed a homogenized continuum model. The foam is assumed to have mass averaged properties between the polymer precursor and the gas bubbles. To model the reactions over time, we follow a kinetic approach. We track moles of water reacted to produce carbon dioxide gas, which leads to the cellular structure of the foam. As the material foams, it is also polymerizes, changing from a liquid to a solid. To understand the dynamics of the foaming process, we start with the equations of motion written for variable density and temperature.

2.1 Equations of Motion

Capturing the evolving volume is critical to understanding foaming dynamics. The continuity equation captures the change in density in space and time, which is the source of foam velocity generation. Here $\boldsymbol{v}$ is the mass-averaged velocity and ρ is the foam mixture density and a function of the volume fraction of gas ϕ, which in turn is a function of temperature, pressure, and gas concentration, and t is time.

$$\frac{\partial \rho}{\partial t} + \boldsymbol{v} \cdot \nabla \rho + \rho \nabla \cdot \boldsymbol{v} = 0 \tag{1}$$

Conservation of momentum takes into account gradients in the fluid stress, $\underline{\underline{\boldsymbol{\tau}}}$, and pressure, p, as well as the effects of gravity, $\boldsymbol{g}$:

$$\rho \frac{\partial \boldsymbol{v}}{\partial t} + \rho \boldsymbol{v} \cdot \nabla \boldsymbol{v} = \nabla \cdot \underline{\underline{\boldsymbol{\tau}}} - \nabla p + \rho \boldsymbol{g} \,. \tag{2}$$

The stress tensor, $\boldsymbol{\tau}$, has a generalized Newtonian shear viscosity, η, in addition to a generalized Newtonian bulk viscosity, κ. The bulk viscosity is associated with the facts that the divergence of the velocity field is non-zero and the flow is dilatational [Bird et al. 1960]. The bulk viscosity term produces only normal stresses and not shear stresses, while the first term produces only shear stresses and no normal stresses.

$$\underline{\underline{\boldsymbol{\tau}}} = \eta \left(\nabla \boldsymbol{v} + \nabla \boldsymbol{v}^t \right) - \left(\frac{2}{3} \eta - \kappa \right) \left(\nabla \cdot \boldsymbol{v} \right) \underline{\underline{\boldsymbol{I}}} \,, \tag{3}$$

where $\left(\nabla \boldsymbol{v} + \nabla \boldsymbol{v}^t \right)$ is the shear rate and $\underline{\underline{\boldsymbol{I}}}$ is the identity matrix. The generalized Newtonian viscosity models imply that the viscosities vary with local fields, but retain a Newtonian form where stress is proportional to strain. Here, both η and κ are functions of temperature, degree of polymerization, and gas bubble volume fraction, as will be discussed later.

Because the process is nonisothermal, an energy balance must be included. The full energy equation for compressible, nonisothermal flow (neglecting viscous dissipation) is:

$$\frac{\partial}{\partial t} \left(\rho C_v T \right) + \left(\nabla \bullet \rho C_v T \boldsymbol{v} \right) = \nabla \bullet \left(k \nabla T \right) - T (\partial p / \partial T)_p (\nabla \bullet \boldsymbol{v}) + \rho T \frac{DC_v}{Dt} + S_{rxn} \,, \tag{4}$$

where T is absolute temperature, C_v is the heat capacity per unit mass at constant volume, and k is thermal conductivity. The energy equation currently used is a subset of the above, in which a constant ρ, C_p (the heat capacity per unit mass at constant pressure), and k are assumed, since compressibility is a second order effect for energy conservation. This leads to a simplified energy equation:

$$\rho C_p \frac{\partial T}{\partial t} + \rho C_p v \bullet \nabla T = \nabla \bullet (k \nabla T) + S_{rxn} \ . \tag{5}$$

Heat is generated by both the exothermic polymerization and foaming reactions (S_{rxn}). The heat of reaction is measured for the foaming and curing system on the wet foam, though the polymerization reaction generates most of the heat since the foaming reaction uses only 4% of the isocyanate by mole:

$$S_{rxn} = \Delta H_{rxn} Y \rho \frac{\partial \xi}{\partial t}, \tag{6}$$

where ΔH_{rxn} is the heat of reaction (energy/mass), Y is the liquid mass fraction, and ξ is the extent of the polymerization reaction.

2.2 Polymerization Kinetics

A convective-diffusion-reaction is written for the extent of reaction for polymerization ξ. The reaction term is written in the form of condensation chemistry [Kamal & Sourour, 1973; Sourour and Kamal, 1976; May 1988; Adolf 1996] and the diffusion is mostly included for numerical stability since this is poorly-behaved hyperbolic equation:

$$\frac{\partial \xi}{\partial t} + v \bullet \nabla \xi + \xi \nabla \bullet v + D \nabla^2 \xi = k(b + \xi^m)(1 - \xi)^n \ . \tag{7}$$

Here b is a fitting parameter, m and n are fitting exponents, and k is an Arrhenius-type rate equation, but also includes the effects of vitrification though a William-Landau-Ferry (WLF) shift factor [William et al., 1955] with a fitting parameter, w. In practice, our formulation is poorly behaved if we include the divergence term which is low order and oscillatory, so we currently ignore it. In future, a better implementation of compressibility may allow us to include this second order effect.

$$k = \left(\frac{1}{\left(1 + w a_T\right)^{\beta}} \right) k_0 e^{E_\xi / RT} \tag{8}$$

where k_o is the rate coefficient, E_ξ is the activation energy, R is the universal gas constant, w and β are fitting parameters, and a_T is the shift factor for time-temperature superposition, which includes an evolving glass transition temperature, T_g, which is dependent on the extent of reaction.

$$\log_{10} a_T = \frac{-C_1\left(T - T_g\right)}{C_2 + T - T_g} \tag{9}$$

C_1 and C_2 are WLF constants that can be found by fitting the shifted data in the rubbery regime [Ferry, 1980]. For T_g we use the Di Benedetto form [Di Benedetto, 1987]. A nice discussion of some other possible forms of T_g for polymerizing systems can be found in Bilyeu et al., [Bilyeu et al., 2001], but we have found the Di Benedetto form works well for our data, fitting its quadratic shape with only one floating parameter.

$$T_g = \frac{T_{g0}\left(1-\xi\right) + A\,\xi\,T_{g\infty}}{\left(1-\xi + A\,\xi\right)} \tag{10}$$

The parameter for the model are T_{g0}, or the glass transition temperature of the unreacted material, $T_{g\infty}$, the glass transition temperature of the fully reacted material, and A, a fitting parameter related to the stoichimetry of the system. T_{g0} and $T_{g\infty}$ can be inferred from experimental data.

2.3 Foaming Kinetics

Polyurethane foam production is a complex process involving reaction of water with isocyanate, which then forms carbamic acid. The acid then decomposes into carbon dioxide. The carbon dioxide is soluble in the polymer precursor and concentrates until it reaches super saturation, at which point nucleation begins. We hypothesize that dissolved air bubbles act as nucleating sites since only minimal foaming occurs unless a sufficient amount of air is incorporated. Once nucleation occurs, the bubbles start to grow.

Our experimental data measures the volumetric expansion of the foam, not the actual concentration of carbon dioxide. Thus we measure an effective carbon dioxide concentration that leads to bubble growth. Unfortunately, this method does not account for the CO_2 solubilized in the polymeric continuous phase or the gas that pressurizes the bubbles after the fluid vitrifies. When fitting the data, we have found that the concentration of carbon dioxide depends only on the concentration of water and is insensitive to the concentration of isocyanate, which is always in excess while the foaming reaction is occurring. This makes sense, since only 3.9 molar % of isocyanate is used in the water reaction. The rest forms urethane and polyamine leaving 15 molar % of the isocyanate unreacted.

We write concentration in terms of moles/volume liquid and track both H_2O and CO_2. Because of the stoichiometry, one mole of water is equivalent to one mole of carbon dioxide, where water is the tracked reactant, with isocyanate being in such excess that it does not need to be tracked. As the water is consumed, it produces carbon dioxide at the same rate.

$$\begin{aligned}
&\frac{\partial C_{H_2O}}{\partial t} + v\bullet\nabla C_{H_2O} + C_{CO_2}\nabla\bullet v + D_{H_20}\nabla^2 C_{H_2O} = -Nk_{H_2O}{C_{H_2O}}^n \\
&\frac{\partial C_{CO_2}}{\partial t} + v\bullet\nabla C_{CO_2} + C_{CO_2}\nabla\bullet v + D_{CO_2}\nabla^2 C_{CO_2} = +Nk_{H_2O}{C_{H_2O}}^n
\end{aligned} \tag{11}$$

As with the polymerization equation, we include the divergence term for completeness but in practice have been unable to include it in the simulations We fit equation (11) to semi-isothermal data for volume evolution with time to determine the rate of reaction, Arrhenius rate coefficient, k_{H_20}, and the rate exponent, n.

$$k_{H_2O} = A_{H_2O} e^{-(E_{H_2O}/RT)} \tag{12}$$

Here k_{H_20} is fit at each temperature and from this a base coefficient, A_{H_20}, is determined along with the activation energy, E_{H_20}. A nucleation time delay, N, must be included to approximate the time required for the carbon dioxide to dissolve in the continuous phase, and then begin nucleating bubbles:

$$N = 0.5\left\{1 + \tanh\left(\frac{t - t_{nucleation}}{t_{nucleation}}\right)\right\}. \tag{13}$$

Without this effect, the shape of the curve is wrong as will be seen in the material parameter fitting section. Best fit parameters for the exponents, n and m, as well as Arrhenius parameters and the characteristic time for nucleation will be given in this section.

2.4 Material Models for Density, Viscosity and Thermal Properties

From the local concentration of CO_2 determined by equation (11), we can determine the volume fraction of gas. We track the molar volume of water and carbon dioxide in the liquid phase only, and then convert to volume fraction of gas, φ.

$$v = \frac{V_{gas}}{V_{liq}} = \frac{M_{CO_2} C_{CO_2}}{\rho_{gas}} \quad \varphi = \frac{v}{1+v} \tag{14}$$

Here the subscript *liq* refers to the polymer phase and *gas* refers to the carbon dioxide, the density of which we define based on the ideal gas law.

$$\rho_{gas} = \frac{P M_{CO_2}}{RT} \tag{15}$$

We can now predict the foam density from the gas density, liquid density, and the gas volume fraction.

$$\rho_{foam} = \rho_{CO_2}\varphi + \rho_{liq}(1-\varphi) \tag{16}$$

The viscosity, η, is a function of both the polymerizing continuous phase and the gas volume fraction. We fit the cure dependence to the rheology measurements for both a dry polyurethane

system that does not foam, representing the polymerizing phase, in a consistent manner to previous systems [Adolf, 2009; Mondy et al., 2010; Rao et al., 2012]. For operating temperatures far above the current glass transition temperature of the reacting polymer, the temperature dependence of the viscosity can be modeled accurately by an Arrhenius relationship [Ferry, 1980]. Dynamic percolation theory predicts a dependence of the Newtonian viscosity on extent of reaction with the form:

$$\eta_0 = \eta_0^0 \exp(\frac{E_\eta}{RT})(\frac{\xi_c^{\,p} - \xi^p}{\xi_c^p})^{-q} \quad . \tag{17}$$

Here the pre-exponential factor η_0^0, the extent of reaction at the gel point ξ_c, the Arrhenius activation energy E_η and dimensionless fitting parameters p and q are determined from fitting exponents to match the data [Martin et al., 1989; Adolf et al., 1990]. Both exponents are positive numbers.

We assume that the foam viscosity follows the Taylor-Mooney form derived from emulsion experiments, extrapolating the discontinuous phase viscosity to zero (for gas) [Prud'homme and Khan, 1996]:

$$\eta = \eta_0 \exp\left(\frac{\varphi}{1-\varphi}\right) \tag{18}$$

where η_0 is the viscosity of the continuous phase as defined by equation (17).

The bulk viscosity is rarely encountered in modeling liquids, which can usually be safely approximated as incompressible, and it is problematic to measure, especially since it is in fact not a true material function for a bubbly liquid but depends on the flow details [Wilson, 1997; Martinez and Kraynik, 1992; Baer and Kraynik, 2005]. We choose to simply assume the relationship between κ and η derived by Baer and Kraynik [Baer and Kraynik, 2005] through mesoscale modeling:

$$\kappa = \frac{4}{3}\eta\left(\frac{1-\varphi}{\varphi}\right) \quad . \tag{19}$$

The energy balance, equation (5) requires C_v, k, and ΔH_{rxn}. The first two quantities can be measured for the final solid foam, and the latter can be measured for the reacting foam mixture in a differential scanning calorimeter (DSC). The heat capacity for a compressible material should be that at a constant volume. We do not know this property as the material is reacting; however, mixture theory [Gibson and Ashby, 1990; Hilyard and Cunningham, 1991] can be used to account for the effect of the evolving gas content based on the properties of the gas and the pure polymer:

$$C_p = \frac{C_{p,liq}\rho_{liq}(1-\varphi) + C_{p,CO_2}\rho_{gas}\varphi}{\rho_{foam}} \tag{20}$$

Evaluation of the former for both an epoxy foam and polyurethane foam [Mondy et al., 2010; Mondy et al., 2014] shows that the effect of gas is small and predicts that the heat capacity per unit mass is virtually independent of the gas content (foam density). If so, we can approximate C_p by measuring the resulting solid foam heat capacity. In contrast, k is quite sensitive to the gas content of the foam and changes significantly during the foaming process.

$$k = \frac{2}{3}\left(\frac{\rho}{\rho_{liq}}\right)k_{liq} + \left(1 - \frac{\rho}{\rho_{liq}}\right)k_{gas} \tag{21}$$

3. FITTING MATERIAL MODELS

Details of the experiments and methods used to populate the foam models can be found in a recent report [Mondy et al., 2014]. Here we summarize some of this information and discuss how we fit the data. Since the report was written, we have developed new kinetic models so the fitting procedures are new.

3.1 Foam Formulation and Properties

The structural foam studied is nominally 10 pcf foam when allowed to freely rise during the expansion phase. The recipes for the BKC 44306 PMDI-10 foam components R and T are shown in Table 1, in parts by weight. The R to T mix ratio is 40.3 to 59.7 parts by weight. The overall formulation is summarized in Table 1. Densities of those components listed with specifications are from the manufacturer supplied data [Dow 2001; SpecialChem 2013].

Table 1. BKC 44306 PMDI-10 Structural Foam Formulation

Material	Specification	PBW	Density at 25°C (g/cm^3)
R-Component (resin)			
Voranol 490 (polyol)	2170369	100	1.109
Water		0.8	0.997
Dabco DC-197 (surfactant)	6500617	1.0	1.01
TMPDA (catalyst)	4604246	0.7	
T-Component			
PAPI 27	4612092	100	1.23

(isocyanate)	
Overall formula	Mass fraction
polyol	0.3932
water	0.0031
surfactant	0.0039
catalyst	0.0027
isocyanate	0.5970

Structural parts are foamed under conditions that vary somewhat depending on the mold size, shape, and features. Typically the two-part material is preheated to 29°C and the mold is preheated to 30-40°C. The material is mixed in fairly large batches (at least 250ml, depending on the size of the mold) with an electric mixer equipped with a blade. The mixed material is immediately poured into the mold, which has been taken out of the oven, and the foam is allowed to rise for about 10 minutes. The mold is then placed in an oven for four hours at a higher temperature, typically 121°C, to complete the cure.

3.2 Kinetics of Polymerization

Micro-Attenuated Total Reflectance (ATR) Infra-Red Spectroscopy (IR) was used to probe the kinetics of polyol isocyanate and related reactions at a range of temperatures. We also examined whether significant differences in spectral features exist that could be used to decouple the polyol cure and water based foaming reaction which competitively consume the isocyanate.

3.2.1 IR Spectroscopy Used to Determine Reaction Kinetics

Micro-ATR experiments were conducted using a heated diamond micro-ATR attachment in a Bruker Equinox 55 IR spectrometer with a DTGS (ID301/8) detector operating at room temperature. Spectra were collected as an average of 64 scans at 4 cm^{-1} resolution. For rapid cure conditions at the higher temperatures (>50^{o}C), we used 16 scans to better capture early reaction kinetics. Repetitive loop macros were used to acquire sequential spectra over multiple hours. The observable spectral features are related to the dominant reactions, namely consumption of the isocyanate at 2260 cm^{-1}, the formation of carbonyls either as urethanes (1723 cm^{-1}) or ureas close to 1700 cm^{-1}, the amide II band at 1521 cm^{-1} and 1510 cm^{-1}, a band at 1308 cm^{-1} and the "urethane ester linkage" at 1218 cm^{-1}. Since the spectra are heavily convoluted, it is not possible to integrate specific band areas for all of these bands. This creates significant constraints for the quantitative analysis of spectral data. While a collective carbonyl band area could be established using a range from 1650-1750 cm^{-1} for integration, all other peak changes were quantified using peak height instead. The spectra also show a decrease of hydroxyls at approximately 3400 cm^{-1} and an increase of NH absorption at 3320 cm^{-1}. Neither one of these broader bands is suitable for simple quantification. Multiple IR bands were examined: carbonyl formation at ~1700cm^{-1}, urethane ester linkage at 1218cm^{-1}, and a non-assigned band at 1308 cm^{-1}. The peak at 1218 cm^{-1} represents the pure curing reaction, as it relates to the C=O-O-R linkage (i.e., the ester side of the urethane) between the polyol and urethane group. Successive

IR spectra were acquired over time (Figure 3), and the relative absorbance changes for specific bands provided time-dependent cure-state information.

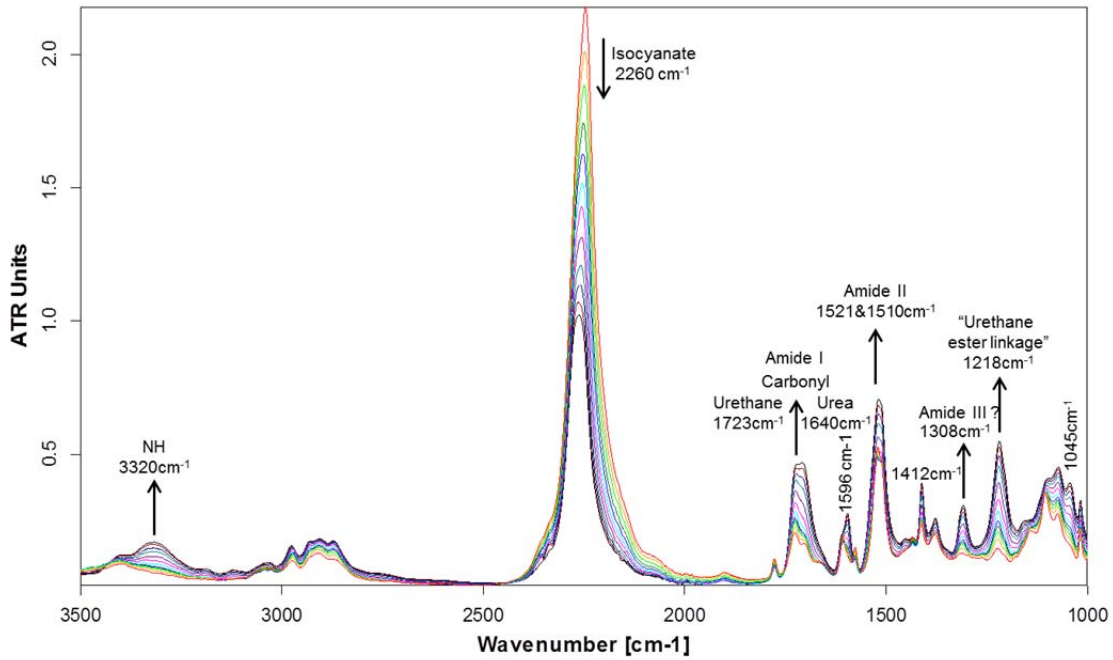

Figure 3. IR-spectra at various times showing the isocyanate peak decreasing as the urethane band and others increase.

A standard sample mass of two grams was mixed, as discussed above, for every run and then placed on the preheated temperature-controlled plate for spectral acquisition. The first spectrum is generated after approximately 64 seconds for 64 scans and 16 seconds for 16 scans. For all dried system experiments, four small beakers filled with anhydrous calcium sulfate were placed around the sample and covered with a beaker, and the sample was covered with a small strip of aluminum foil to minimize any diffusion of water into the sample. Wet foam experiments were treated in a similar manner.

For the PMDI foam under investigation, the isocyanate reactions on a molar basis split into 94.4% for the polyol addition to form urethanes, and roughly 5.6% for the isocyanate water foaming reaction. In principle, approximately 5.6% of urea formation from an amine isocyanate addition reaction should be observable as a follow-up of the CO_2 producing carbamic acid decomposition.

Two resin systems were evaluated: The basic foam system consisting of a standard foam system in which the polyol component contains a pre-mixed surfactant, water and catalyst, and a "dried" system from which the water had been removed from the polyol component using common laboratory-grade zeolites as a drying agent. In principle, a comparison of the spectral features between a dried non-foaming system, and a water-containing polyurethane foam system should reveal spectral variations in the nature and quantity of the underlying reactions. The dried system should exclusively display a dominant urethane formation, while the wet system should

involve a combination of urethane and urea products. However, both systems will be further convoluted by subsequent allophanate and biuret reactions when isocyanates are used in slight excess. This mix of reactions implies that a deconvolution of the foaming and urethane cure reactions based on IR spectral features alone is intrinsically difficult. A complicating issue is that the carbonyl group of the urea does not display a specific isolated spectral band, but only appears at a slightly lower wave-number than the urethane carbonyl. Deconvolution of the urethane and urea carbonyls, particularly at low concentrations of urea is prohibitive, unless chemometrics and sophisticated algorithms are applied. Such approaches were not the goal of this overview study.

To determine curing rates in the full water-containing foam system, IR data were obtained for the 1218 cm^{-1} band height as a function of time and temperature (Figure 4).

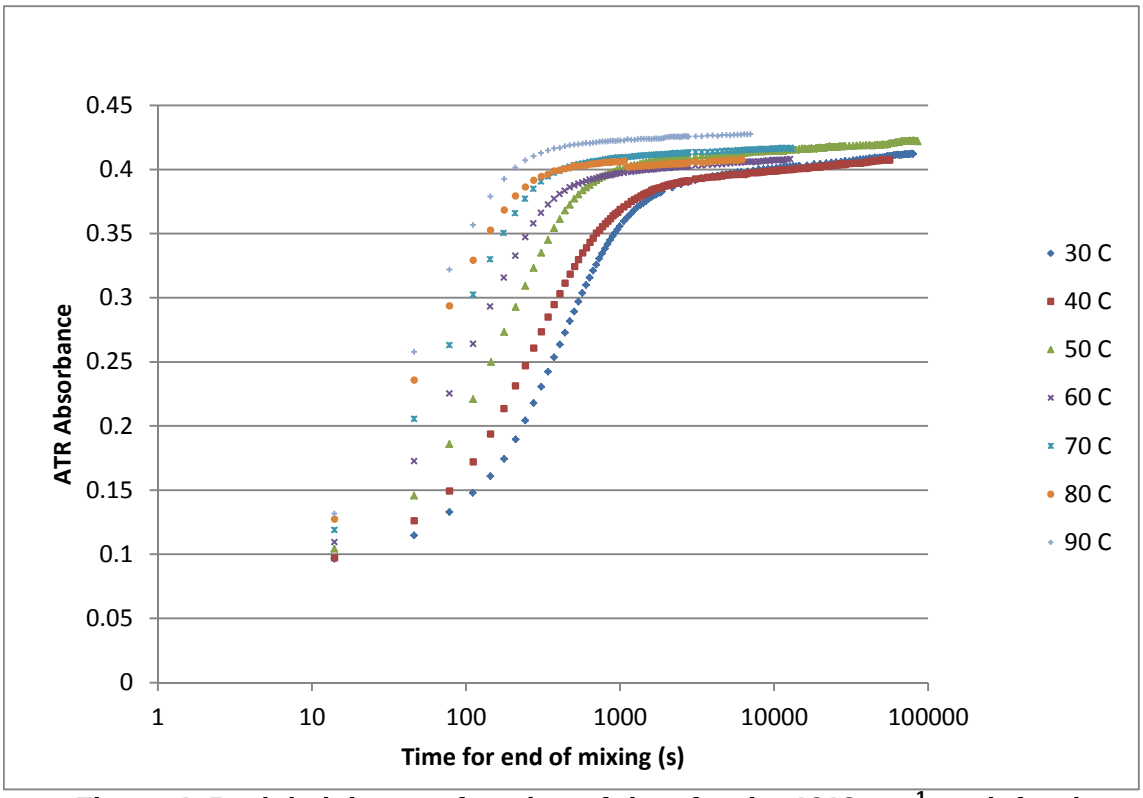

Figure 4. Peak height as a function of time for the 1218 cm^{-1} peak for the wet PMDI material. Isothermal tests were carried out for various temperatures ranging from 30°C to 90°C.

The raw peak height from Figure 4 can be normalized by the maximum peak height, which we assume to be roughly ~0.6cm^{-1}.The normalized height is a direct measure of the extent of reaction as a function of time and temperature. Shifting the various temperature data to obtain a master curve (Figure 5) gives shift factors as a function of temperature, which can then be used to determine the activation energy for the Arrhenius rate constant.

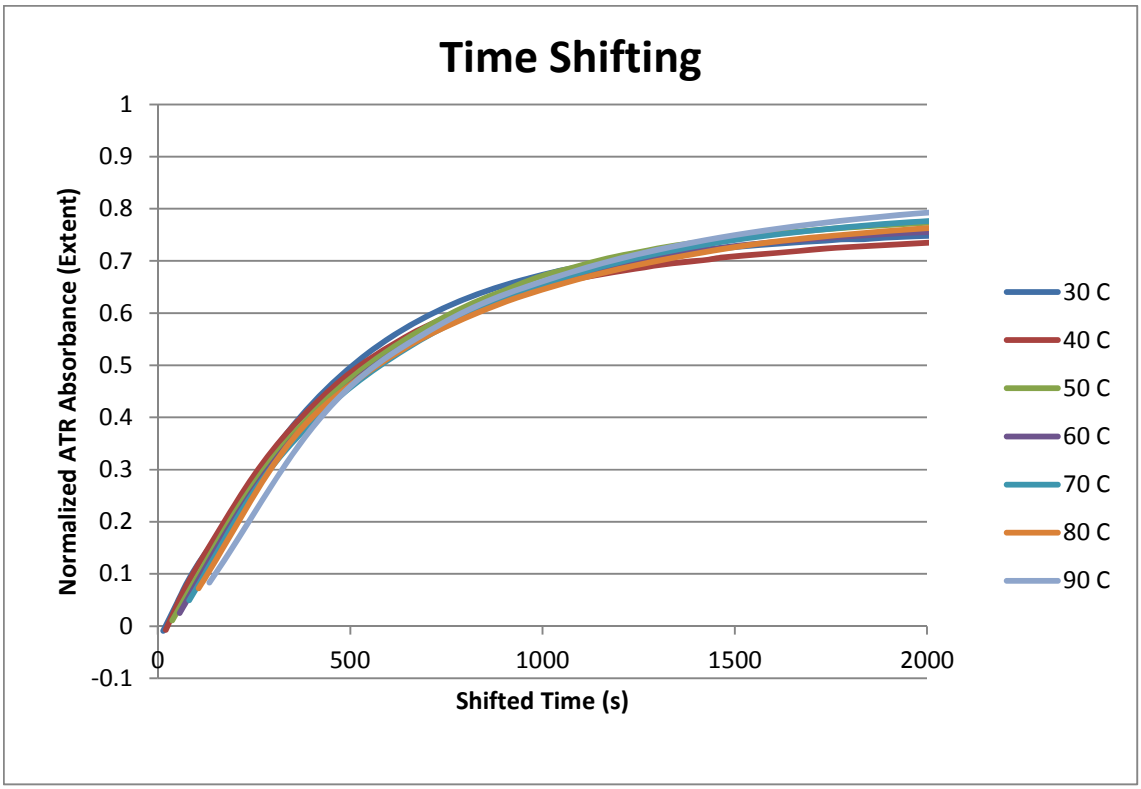

Figure 5. Shifted extent of reaction for isothermal tests carried out for various temperatures ranging from 30°C to 90°C. The shift to a master curve works well up until 1-2 hours.

Figure 6 shows a plot of the natural logarithm of the shift factors versus the inverse of temperature in Kelvin. The slope of this linear plot gives the activation energy, E_η/R, for the rate constant.

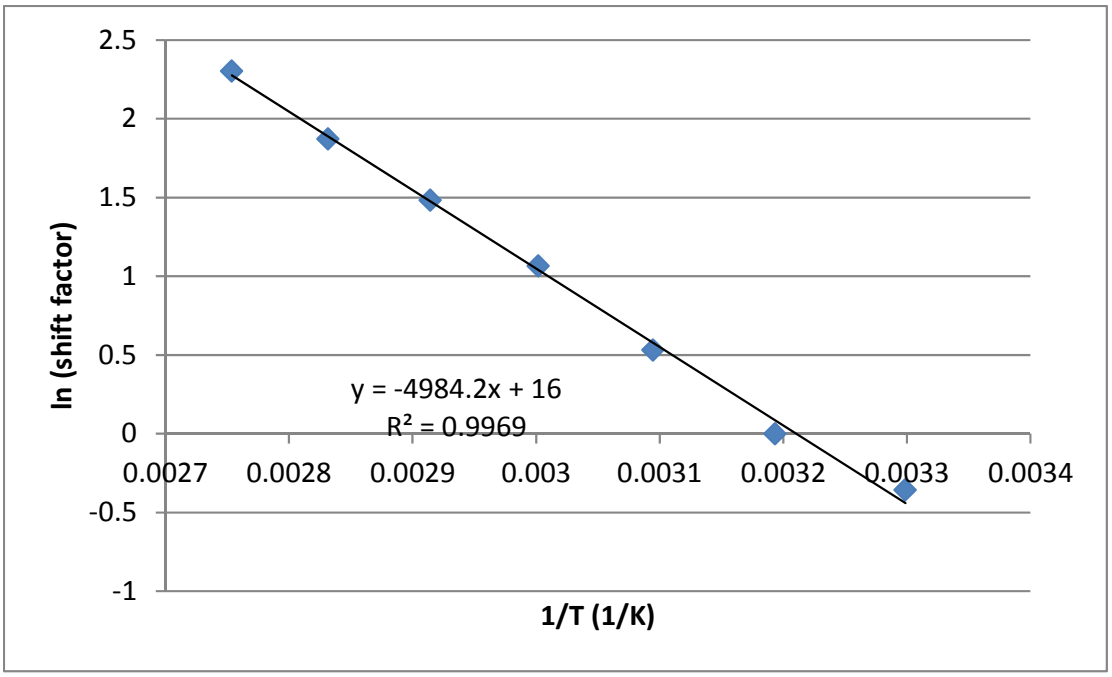

Figure 6. The natural log of the shift factor plotted versus the reciprocal temperature in Kelvin, gives the activation energy, E_η/R = 4984.2 K, for the Arrhenius rate constant for the polymerization reaction.

Once the extent of reaction and activation energy are determined, the reaction kinetics (e.g. rate constant and order of reaction) can be obtained by fitting equations (7)-(10) for the early time data. This is done using the extent and the rate extent, formed by numerically differencing the extent data, and then fitting this data to equation (7) assuming no advection or diffusion or cure gradients exist in the small IR samples. For this step we ignore vitrification. The evolution of the glass transition temperature must be included to capture the late time data and the different final extent of reaction for different temperatures. An estimate for T_g is determined from rheology and DSC. This will be discussed in the next sub-section.

3.2.2 Parameter fitting for polymerization kinetics

A rough value of k=0.0014 s^{-1} at 23°C, combined with the Arrhenius fit from Figure 6, yields a value for k_0 of 1951.8 s^{-1}. This value seems to capture the temperature dependency well. The best values to fit the orders of reaction are n=2.0 and m=0.2. The heat of reaction, ΔH_{rxn}, was measured from DSC for the wet and dry foam, which had similar values of 181 J/g. The summary of the parameter values for the epoxy polymerization kinetics are summarized in Table 2.

Table 2. Polyurethane Polymerization Kinetic Parameters

Polyurethane Cure Parameter	**Value**
Rate coefficient, k_0	1951.8 s^{-1}
Universal gas constant, R	8.31 J/mol K
Normalized activation energy, E_η/R	4984 K
Activation energy, E_η	41.4 kJ/mol
Rate parameter, b	0.6
Rate exponent, m	0.2
Rate exponent, n	2.0
Heat of reaction, ΔH_{rxn}	181 J/g
Glass transition temperature at zero cure, T_{g0}	250K
Glass transition temperature at zero cure, $T_{g\infty}$	405K
Glass transition evolution parameter, A	0.35
WLF parameter, C_1	25
WLF parameter, C_2	30
WLF scaling parameter, w	0.2
WLF scaling exponent, β	0.2

We simultaneously fit the extent and the rate to insure that both a fairly good representation of the curing reactions for all temperatures. The extent is used for the viscosity fit and the rate is used in the energy equation to track the heat generation from the reaction, so representing them both accurately is important to the modeling effort. Comparison of the theory, using the parameters listed in Table 2, to data is shown in Figure 7 and Figure 8. If we focus on getting a good fit for the lower temperatures associated with processing, then it is hard to capture the higher temperatures.

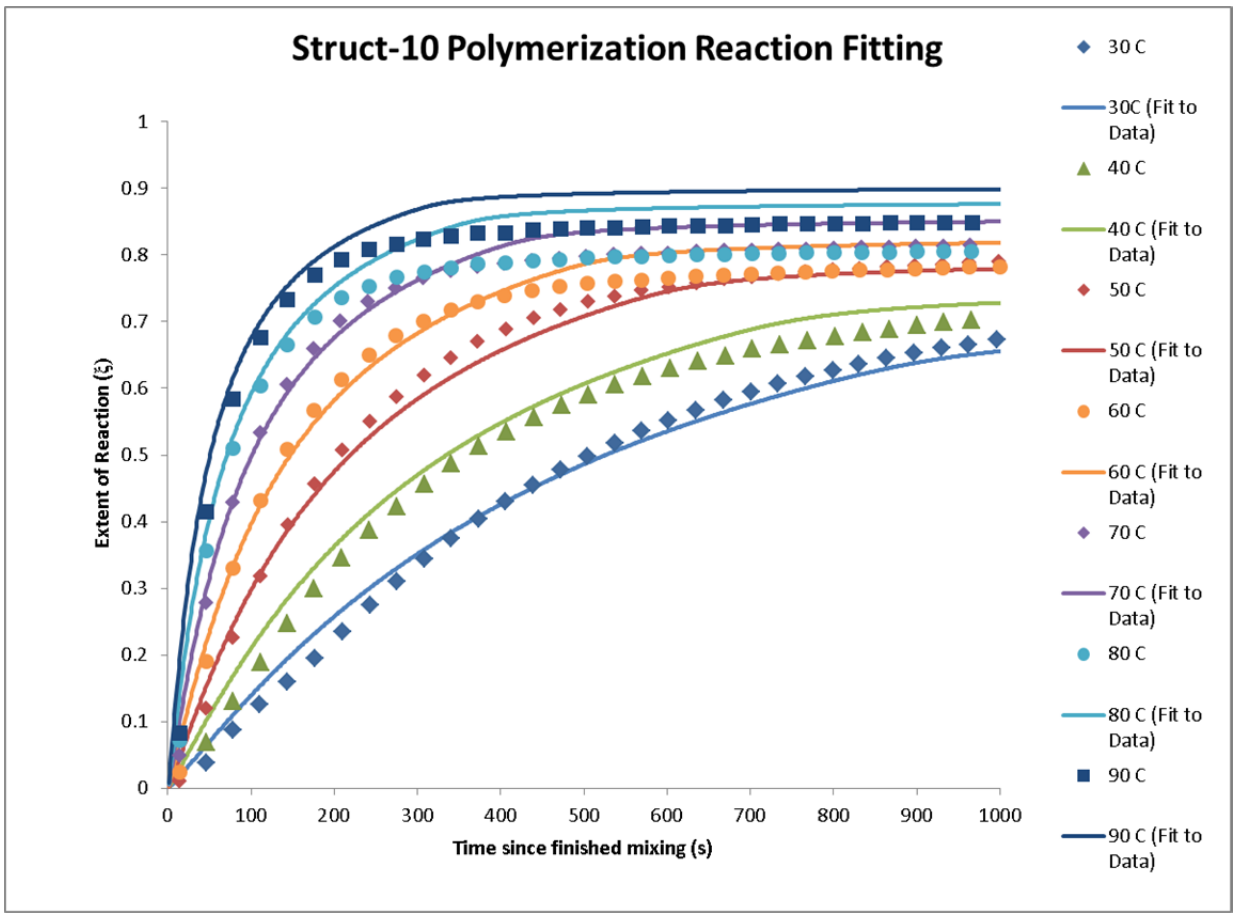

Figure 7. The measured extent of reaction compared to the numerical fit from equation (7) for seven different temperatures.

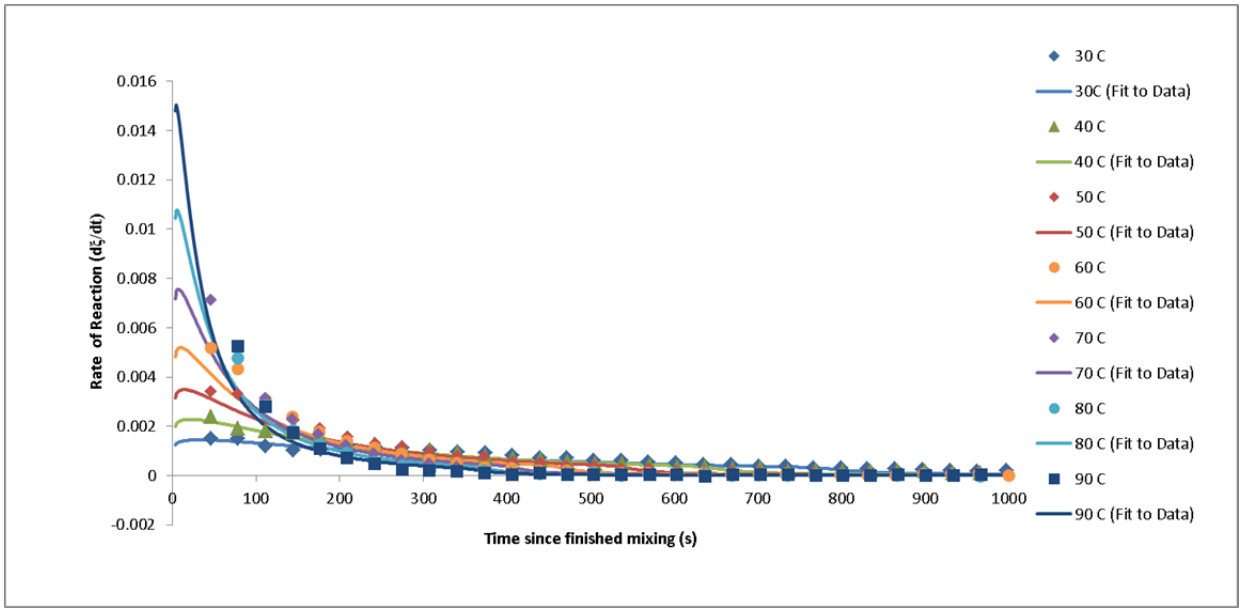

Figure 8. The rate of reaction compared to the numerical fit from equation (7) for seven different temperatures.

Between gelation and vitrification the reaction rate decreases because reactants become less mobile due to solidification of the polymer. We represent this phenomenon using an evolving glass transition temperature and a shift factor. The evolution of the glass transition temperature with extent of reaction is fit using viscosity vitrification data and differential scanning calorimetry (DSC) data. The rheology of the dry PMDI material is discussed below (Section 3.4.1). The time that the viscosity became too large to measure was taken as an estimate of the vitrification time. Because both these and the Micro-ATR experiments were isothermal, the time of the rheology measurement could be directly translated into an extent of reaction in the Micro-ATR experiment at the same temperature and then fit to equation 10 with educated guesses for reasonable parameters T_{g0} and $T_{g\infty}$.

We also use transient DSC to indirectly observe the onset of the glass transition in the curing dry PMDI material and correlate the observed glass transition onset with a state of cure (network connectivity and cross-link density). This allows us to test a larger range of temperatures than the rheology does, as well as having an independent confirmation of the T_g model. A batch of dry PMDI is prepared, measured into DSC pans which are each crimped shut, and then immediately put into the deep freeze to minimize the amount of curing that occurs during specimen preparation. At test time, a specimen is removed from the deep freeze, placed in the DSC at 25°C, and immediately quenched to -30°C. This step is important to prevent condensation from forming on the outside of the specimen pan. After the temperature has equilibrated at -30°C for 5 minutes, the specimen is subjected to a series of cyclic temperature ramps, hold, and cooling ramps back at -5°C. The temperature rate and maximum temperature are experimental variables that may be changed from test to test. We frequently used 10°C/minute for heating and cooling ramps and hold times at the high temperature target (50°C, 55°C, and 60°C) of 1 minute.

During these temperature ramps, the heat flow relative to the reference pan, which is the standard definition in DSC, is measured. On heating, we can clearly observe the transition from the glassy

state to either the rubbery state (increase in endotherm per degree ^{o}C), which is followed by a significant exotherm due to curing, or we directly observed a transition from the glassy state to a state with a substantial curing exotherm. (The exotherm is caused by heat generated by the polymerization reaction.) The onset of additional cure is easily observed because, especially during the first two cycles, the endothermic curve has an extremum as the reaction suddenly restarts. Ahead of this extremum, an inflection point may be calculated from the endothermic curve during specimen heating. Therefore, for a given specimen, the time since the start of the cyclic DSC test is recorded at the locations of these extrema and inflection points.

Given the cure kinetics and T_g parameters above, we can integrate the non-linear reaction kinetics ordinary differential equation using the time-temperature history applied to a specimen during the transient DSC test. We can associate specific time-temperature histories with extent of reactions. Finally, we can plot these points of T_g onset vs. extent of reaction with the T_g vs. extent of reaction used in the Di Benedetto fit. If the agreement is good, then the analysis can be considered a validation of the reaction kinetics fit and Di Benedetto form. However, if the agreement is poor, then we must reevaluate the Di Benedetto parameters to try to improve the fit. Each time the parameters are adjusted, the reaction extent must be re-integrated from the time-temperature histories for each specimen.

An example of the raw DSC data and with some kinetics analysis is shown in Figure 9. The specimen was subjected to heating and cooling rates of 10^{o}C/min to a target temperature of 50^{o}C. Then, after 10 cycles, the specimen was heated to 100^{o}C to determine the glass transition onset after the ten cycles. The first part of the figure shows the raw heat flow versus temperature data (with the time axis removed). The inflection and extremum for the first heating ramp are marked.

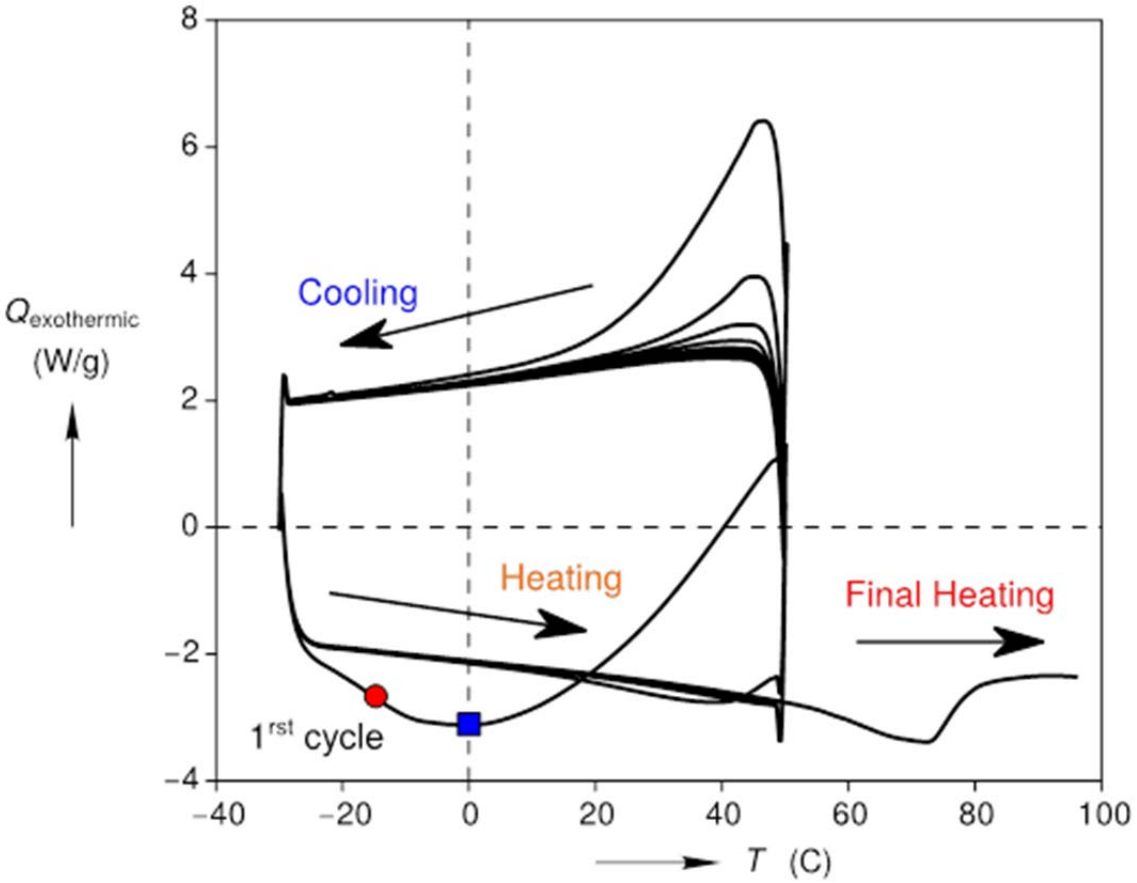

Figure 9. An example of raw DSC data from thermal cycling of dry polyurethane.

Then, the reaction kinetics are integrated with this time-temperature history, which results in a reaction extent versus time for this non-isothermal history (Figure 10). The locations of the inflection and extrema are also placed on this curve, and the temperature vs. time is also plotted for reference.

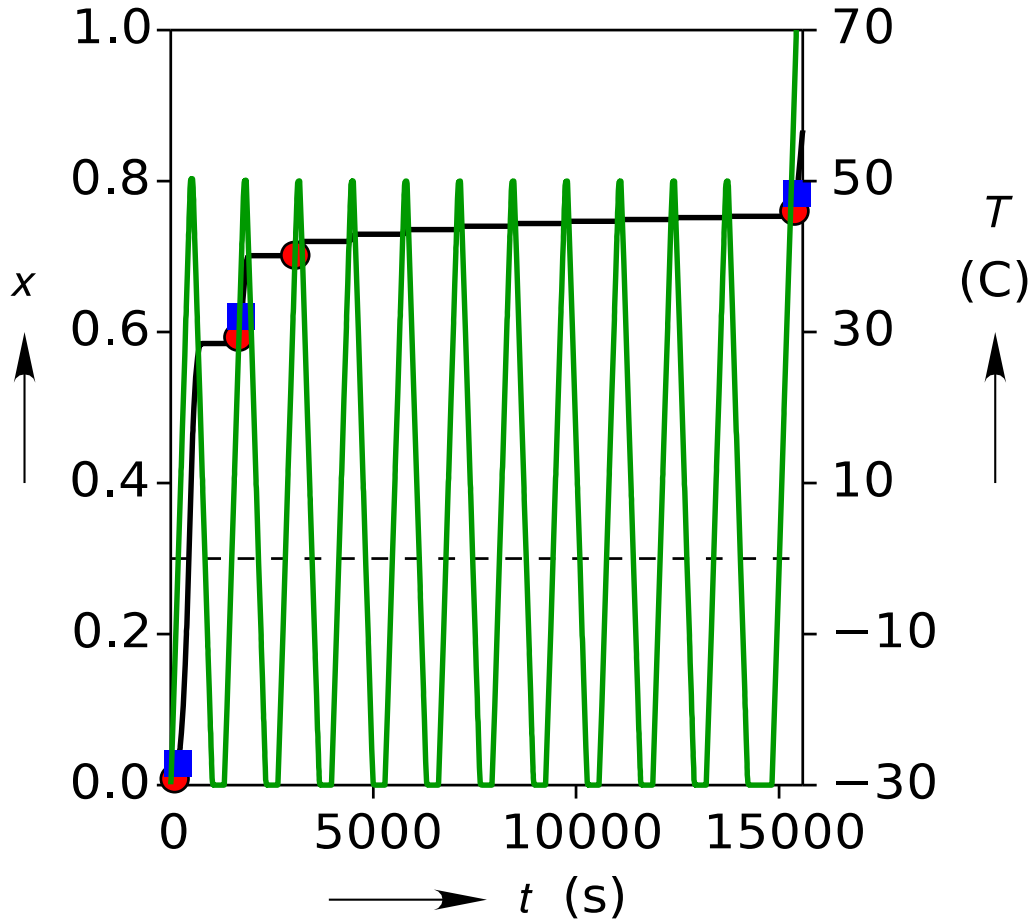

Figure 10. Estimate of T_g with extent of reaction

Finally, these T_g onset locations along with the rheological estimates of vitrification extent are plotted against reaction extent in Figure 11 to test the Di Benedetto fit. Happily the DSC and rheological vitrification data agree quite well. Including vitrification is very important since we are modeling the post-gelation curing, as discussed in a companion report [Long et al., 2015]. If vitrification is not included, the reaction will go to completion for all temperatures. Vitrification quenches the cure and leaves cure gradients in place.

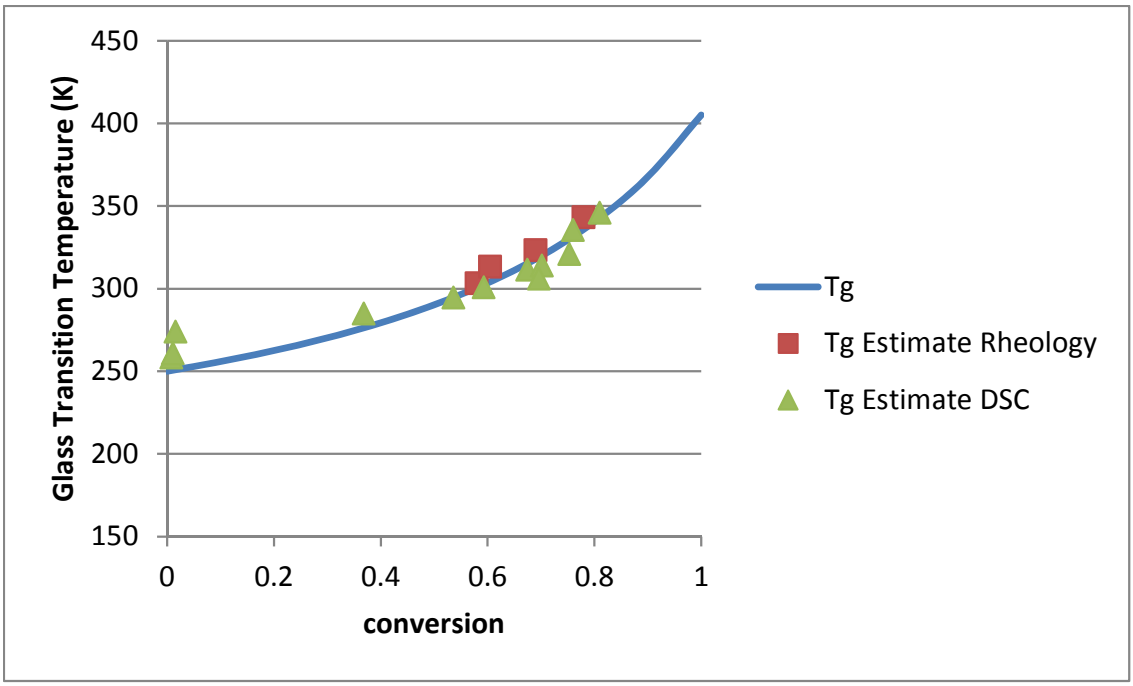

Figure 11. Glass transition temperature evolution with extent of reaction fit to a Di Benedetto model using rheology and DSC data.

3.3 Foaming Reaction

Unfortunately, no specific peak in the IR spectrum exists for the foaming reaction for two reasons. First, the carbamic acid generating the CO_2 is a transient species, and second, the carbamic acid decomposition results in urea linkages (carbonyl and amide groups), which overlap with the urethanes in the spectrum. Therefore, a different method must be used to determine the foaming reaction rates, as will be discussed in the following subsection.

3.3.1 Experiments to determine foaming kinetics

In order to estimate the rate of gas formation, we observe the height evolution of a foam column with time and assume that the increase in volume is solely due to the production of CO_2. This method is useful since it predicts the apparent CO_2 generation that goes into volume generation. However, it does not account for all the CO_2 produced, since some is lost to the atmosphere through the free surface, some is remains supersaturated in in the polymer, and some leads to bubble pressurization. All of these secondary CO_2 pathways do not produce an increase in volume. Because the reaction is exothermic and the foam precursor materials cannot be preheated to high temperatures (excessive preheat causes the water to evaporate so it will not be available for the foaming reaction), these height evolution experiments cannot be performed under isothermal conditions, unlike the IR spectrophotometry. We also hypothesize that the blowing reaction could produce pressurized bubbles, especially between gelation and vitrification of the continuous phase. Therefore, not only volume change, but also temperature and pressure are measured. The number of moles of CO_2 is then estimated through the ideal gas law:

$$pV = n_{CO_2} RT \tag{22}$$

where V is volume of gas measured in the foam experiment. The method assumes that the volume change due to temperature of the liquid phase is negligible, as is any volume change from reactions not producing gas.

All tests are performed in an oven, where the mold is preheated to the desired testing temperature. For all tests the precursor foam material is preheated to 30°C. The material is mixed for 45s inside the injection syringe with an overhead mixer fitted with a small spatula rotating at 1800 rpm. Mixing directly in the injection syringe provides significantly faster transfer of the material into the mold after mixing.

Figure 12 shows frames from a typical front-tracking video at an oven temperature of 30°C. Note that the foam started expanding in such a short time that it was difficult to capture the initial time data, even at this relatively low temperature where the reactions are slower.

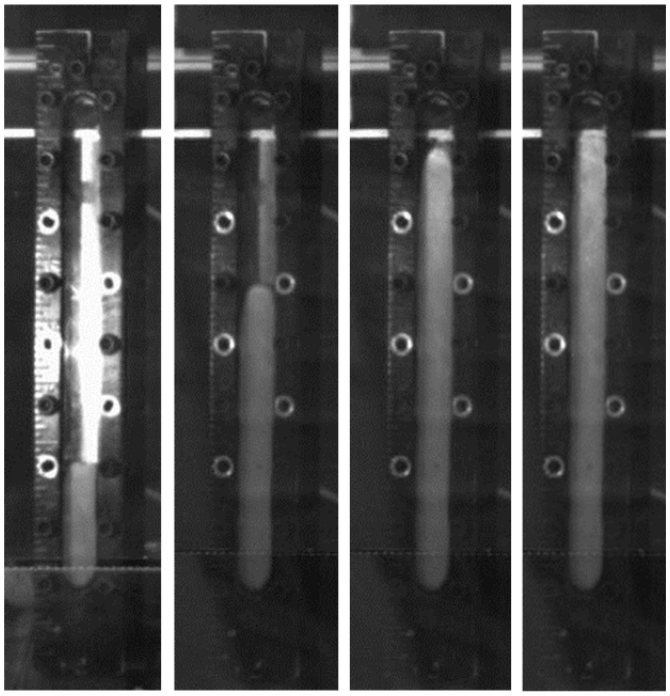

Figure 12. Video frames showing structural foam PMDI-10 expanding in a bar mold at 30 °C. The frames correspond to time= 13, 73, 158, and 245 s after the end of mixing the resin and the curative together for 45 seconds. Even at this relatively low temperature the foam had expanded significantly within the 13 seconds that it took to load the syringe injector and get the material into the mold.

Individual frames are analyzed with image processing software (Image Pro Plus, Media Cybernetics, Rockville, MD) to determine the height evolution with time, calibrated with the known dimensions of the channel. Knowing those dimensions of the channel, we can convert the height of the foam to volume, and knowing the mass injected we can convert the volume to an overall density. Assuming volume change is caused by the generation of CO_2 gas and possible expansion or contraction of the gas due to temperature; we can calculate the generation rate of the gas forming reaction.

Example data are shown for the case of an oven temperature of 50°C in Figure 13 and **Error! Reference source not found.**. Note that the temperature peaks before the foam stops expanding. The temperature rise is caused by the heat of reaction. Note also that the pressure peaks after the foam stops expanding; implying that the bubbles may become pressurized after the polymerization restrains the bubble expansion. However, the pressure is measured at the wall, and it is not clear how that pressure is related to that within the bubbles. For lack of a better estimate, we use this wall pressure to calculate the moles of gas.

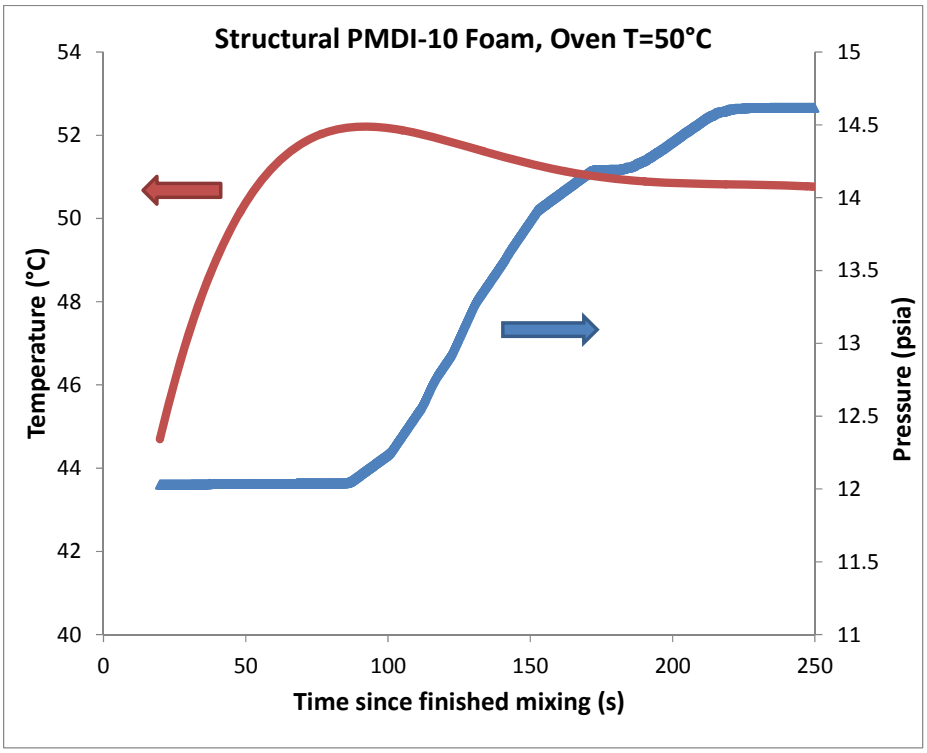

Figure 13. Temperature and pressure measurements used to calculate the number of moles of CO_2 produced at a nominal temperature of 50°C.

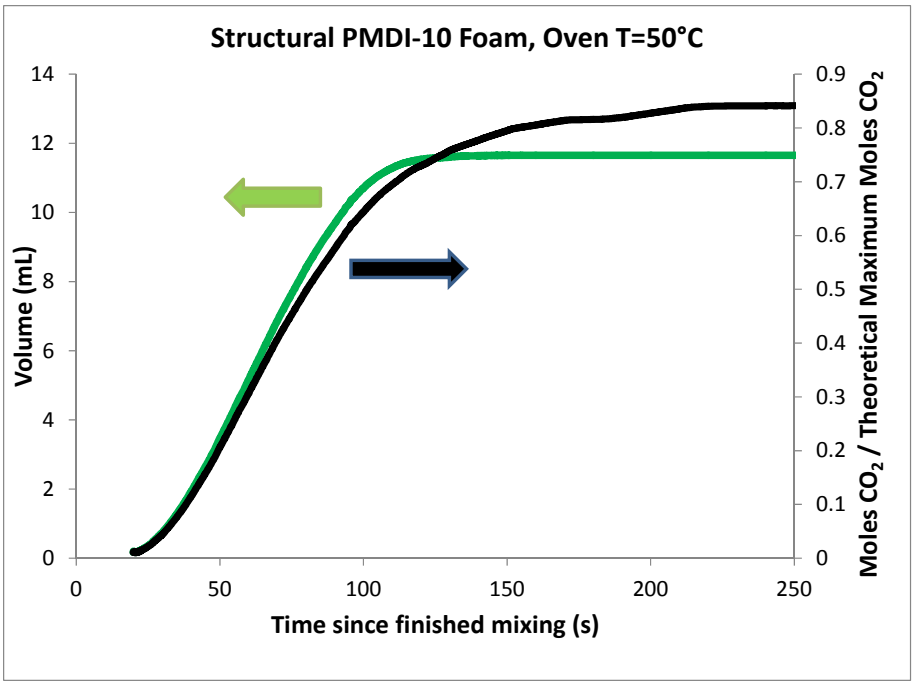

Figure 14. Measured volume and the moles of CO_2 produced calculated from the ideal gas law.

3.3.2 Parameter fitting for foaming kinetics

In the experiment, 3.59g of foam precursor is injected giving an injection volume of 3.38 cc assuming an initial density of 1.06 g/cc. The volume is difficult to estimate because the foaming begins very quickly. We use a solubility estimate of 0.018 cc STP CO_2/(cc polymer *P(cm Hg)) [Celina, 2013] giving a maximum solubility of 0.05 mmol/cc. We make an assumption that roughly 0.01 mmol/cc is the non-volume creating carbon dioxide that is still dissolved in the continuous phase and use this value for all temperatures. This is an assumption, since we know that the solubility is temperature and pressure dependent. In future studies, we would like to include rate equation both for the gas-phase carbon dioxide as well as the solubilized carbon dioxide. For now, we assume that 0.01 mmol/cc of water is unavailable to produce CO_2 bubbles because this amount is dissolved in the liquid.

As there is an excessive amount of isocyanate, the limiting reactant to produce CO_2 is water. One mole of CO_2 is produced from each mole of water (H_2O) in the foam kit formulation. Note that this assumes that there is no additional water absorbed into the resin components as received from the manufacturers or that water is not absorbed or lost to the atmosphere during storage or processing.

Table 3 gives the molar information for each reactant used to fit the data, including the molecular weights and the initial molar concentration of the reactants. The maximum amount of carbon dioxide that can be produced is limited by the initial concentration of water. We assume that the initial concentration of CO_2 is a small but nonzero (starting from zero concentration makes the equations overly stiff to integrate) and include the air only as an effect on the initial density of the mixture, though we estimate the foam precursor contains at least 14 vol% air bubbles before nucleation begins.

Table 3. Molar Volumes of Reactants (mmol/cc)

Component	Molecular weight	Initial moles (mols)	Concentration (mmol/cc)
Polyol	460	0.003089	0.9128
Water	18.02	0.000631	0.1854
Isocyanate	340	0.006346	1.875
Carbon dioxide	44.01	0.000051	0.015

Figure 15 shows the Arrhenius fit for the four temperatures for which we have data, which gives the activation energy of the foaming reaction of E_{H2O}/R = 5095.8 K.

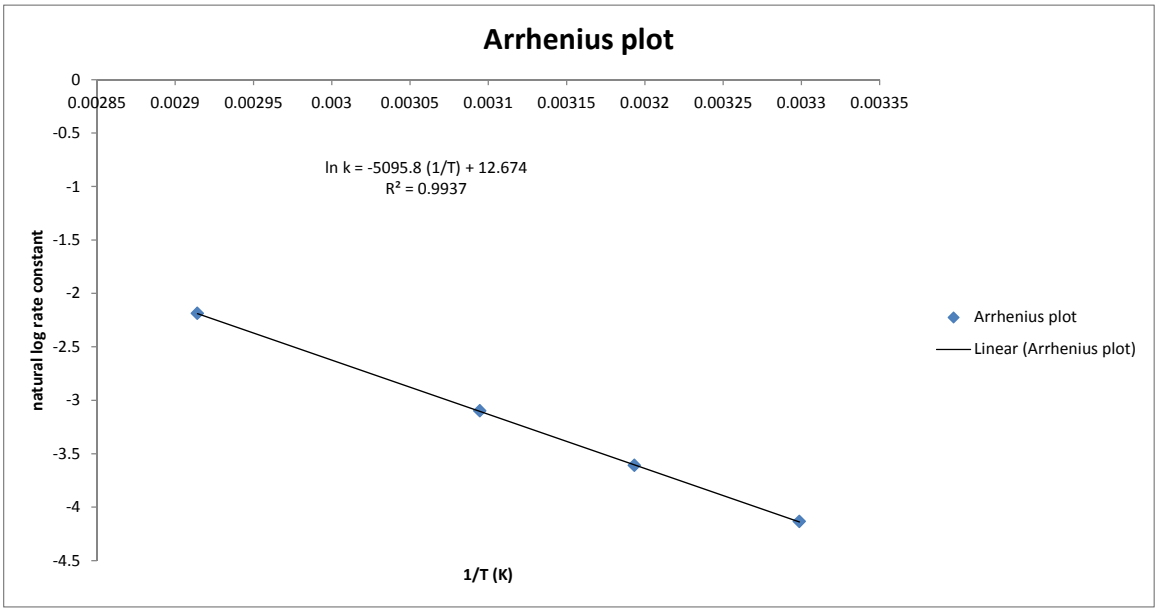

Figure 15. Arrhenius behavior for the carbon dioxide rate equation.

Figure 16 compares the measured water concentration to the predictions from the model. The results agree fairly well with the data at early times, though the reaction slows more at later times. This is probably due to the fact that bubbles have trouble growing at later times as the material becomes more viscous, then viscoelastic, and finally vitrifies to a solid. It is difficult to capture this effect without a bubble-scale model.

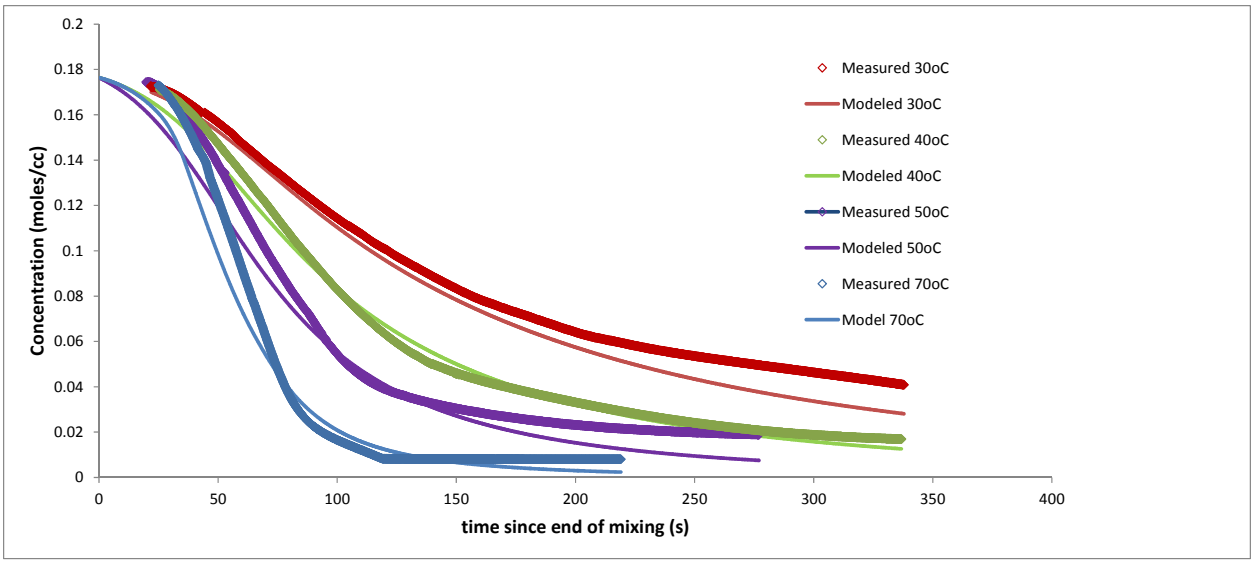

Figure 16. Model compared to data for BKC 44306 PMDI-10 foam at an oven temperature of 30°C, 40°C, 50°C and 70°C.

The measured values of the rates of water consumption have more scatter in them but with the inclusion of nucleation time, we can capture the change in the shape of curve, allowing us to capture the early time data when the carbon dioxide formation does not lead to volume change. A simple rate equation would not capture the complexity of the data. Figure 17 shows the rate data compared to the model predictions for rate for three temperatures 30°C, 40°C and 50°C. The data for 70°C was very hard to fit because the data had a highly variable temperature ranging from 30°C to 70°C.

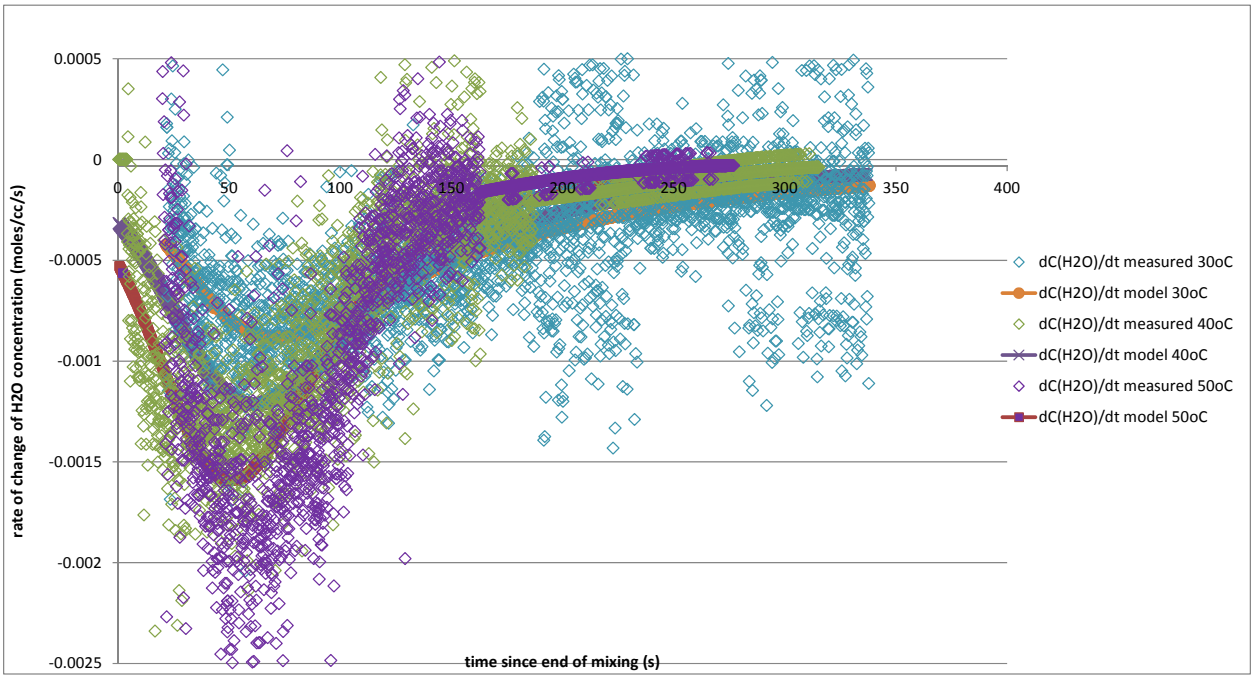

Figure 17. Model rate predictions compared to rate data for BKC 44306 PMDI-10 foam at an oven temperature of 30°C, 40°C, and 50°C.

We use variable temperature to estimate the response using the Arrhenius fit from the other temperatures and the actual temperature and pressure from the data. The nucleation time should probably vary with temperature, since the time scale is a bit off. The fit and data are seen for 70^{o}C in Figure 18.

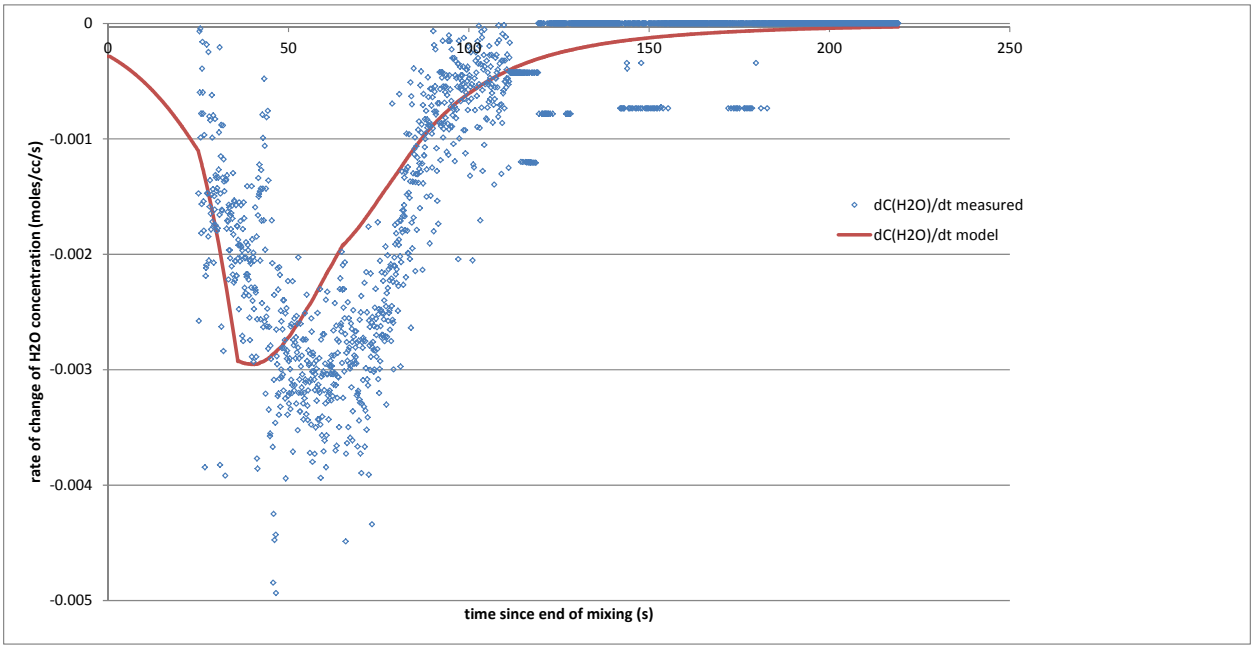

Figure 18. Model rate predictions compared to rate data for BKC 44306 PMDI-10 foam at an oven temperature of 70°C.

The predicted density versus time for 30^{o}C is shown in Figure 19.

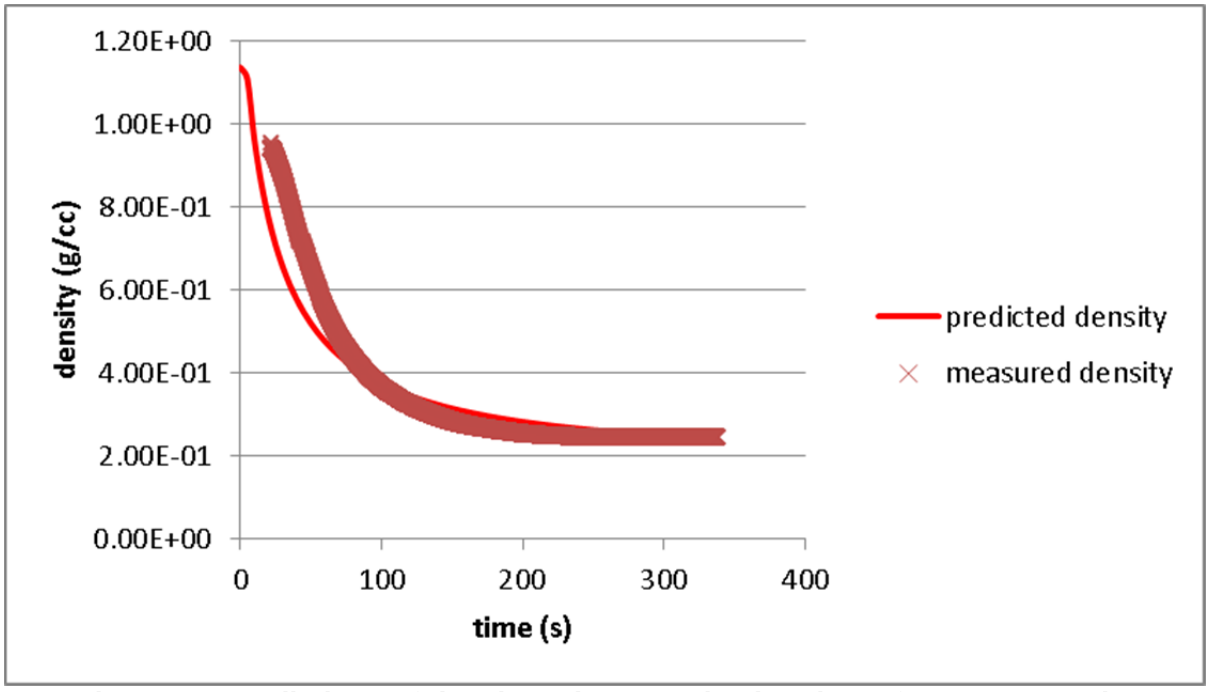

Figure 19. Predictions of density using a nucleation time of 40s compared to measured density with time in the channel for 30°C.

The coefficients for the gas generation kinetics model are summarized in Table 4.

Table 4. Gas Production Kinetic Parameters

Gas Production Parameter	**Value**
Rate coefficient, A	3.168e5 $s^{-1}[mmol/cc]^{-n}$
Normalized activation energy, E_a/R	5095.8 K
Activation energy, E_a	42.35 kJ/mol
Rate exponent, n	1.35
Nucleation time, t_{nuc}	40s

3.4 Rheology Fitting

Foam rheological properties are complex, exhibiting effects of changing microstructure as bubble growth or breakage occurs due to coalescence or shear. However, here we will assume that the gross foam rheology can be approximated with an apparent viscosity and slip at the wall. The suspension/emulsion literature has clearly shown that the effects of the continuous phase are separable from the discontinuous particle, emulsion, or gas bubble phases [Prud'homme and Khan, 1996]. For this reason, we have chosen to separate the viscosity into two parts dependent on 1) continuous phase polymer properties, dependent on extent of reaction and temperature, 2) gas bubble volume fraction. We assume these components are multiplicative and can be decoupled.

3.4.1 Dynamic Viscosity of the Continuous Phase

The goal of characterizing the rheology of the dry material is to estimate the viscosity of the continuous phase, η_{cure}. The components are preheated to 30°C. The rheometer plates are preheated to the operating temperature so that the material will quickly reach that temperature once loaded onto the bottom plate. Nevertheless, it takes time (roughly 60 to 90 s) to load the material. The oscillatory stress was controlled at values ranging from 0.1 to 10 Pa (at 1 Hz) and showed no significant effect of the stress value, indicating that we were within the linear viscoelastic regime. Complex moduli were measured at four temperatures (30, 40, 50, 70°C) and a dynamic viscosity was determined.

The temperature dependence of the curing viscosity and its Arrhenius parameters were determined by shifting the data to achieve a master curve [Mondy et al., 2014]. The shift can be somewhat arbitrary depending on whether we focus the master curve on the early or late times. This particular shift was chosen to overlay the viscosity plots for the most time possible. Figure 20 shows the shift factor versus inverse temperature to determine the temperature dependence of the curing viscosity, giving an E_η/R of -1549.4 K.

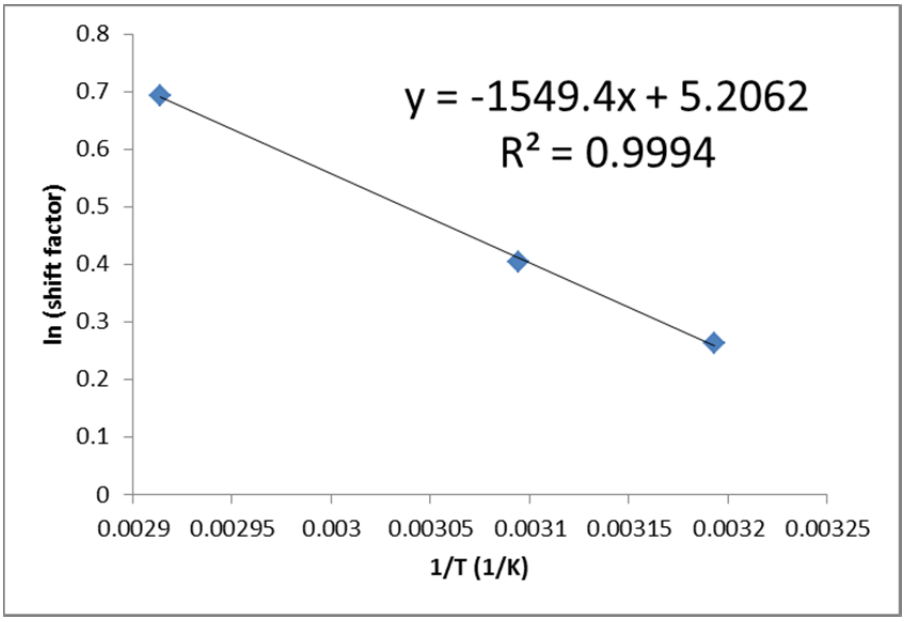

Figure 20. Activation energy (E_η /R) given from viscosity time shift factors. Here, E_η/R=-1549.4 K

Using this activation energy, the other parameters were fit to the data by plotting and trying to maintain a good fit for all temperatures and especially at early times. Experimental results are given in Figure 21 for the viscosity at four temperatures and compared to the viscosity fit for the curing polymer phase.

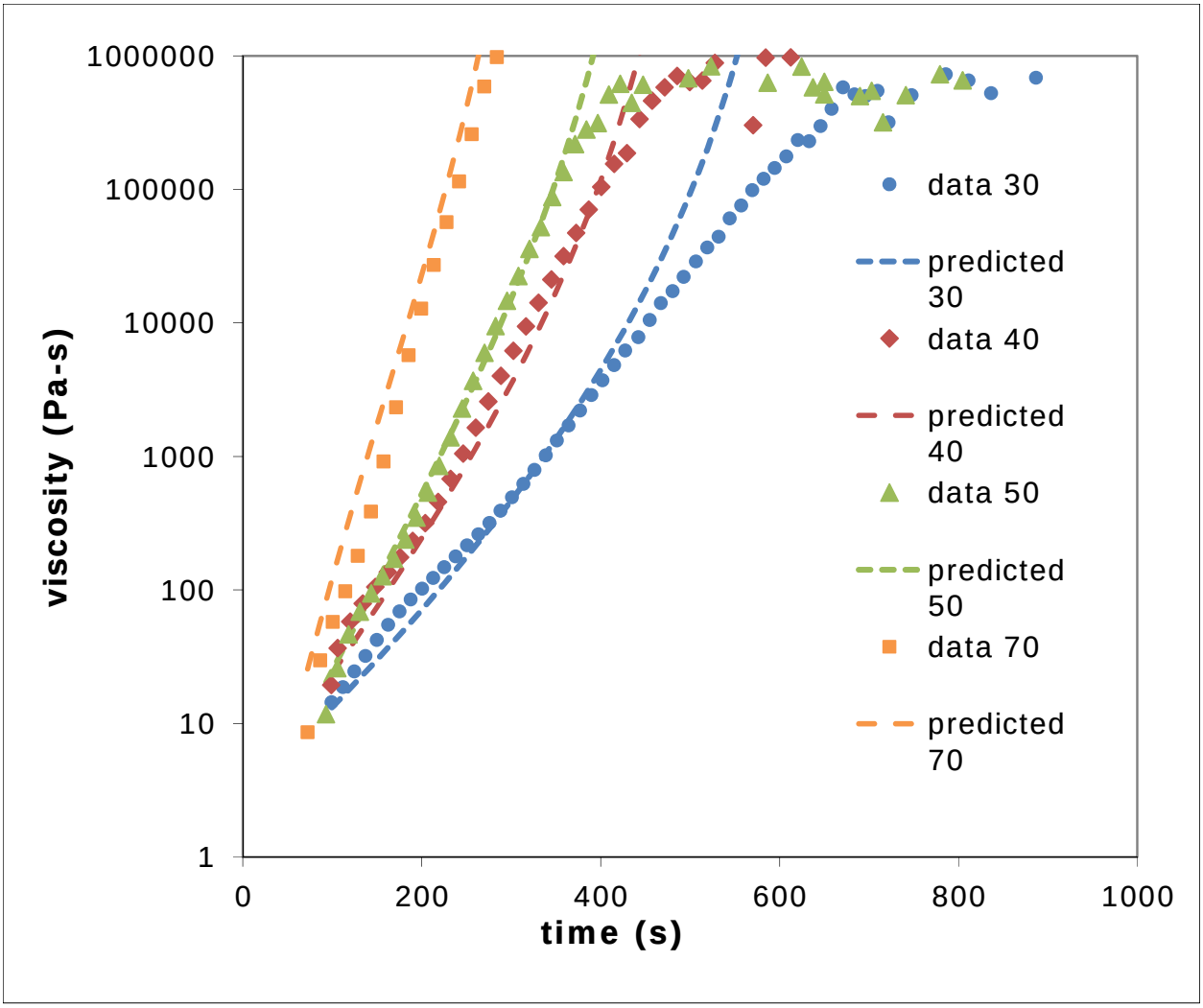

Figure 21. Viscosity for dry polyurethane at 30°C, 40°C, 50°C, and 70°C. The data is compared to the curing viscosity fit.

The parameters used to populate this model are given in Table 5. With these nonlinear equations, multiple values of the parameters can give similar agreement with data.

Table 5. Curing Viscosity Model Parameters

Curing Viscosity Model Parameter	Value
Uncured viscosity at reference T, η_{00}	600 Pa s
Normalized activation energy, E_η/R	-1549.4 K
Activation energy, E_η	12.88 kJ/mol
Extent of reaction at gel point, ξ_c	0.6-.86 (used 0.86 in the code)
Curing viscosity exponent, p	1.0
Curing viscosity exponent, b	5.0 (used 6.0 in the code)

The gel point increases with temperature and can be fit to a linear or quadratic model. Here we use a more complex form to ensure the values stay between 0 and 1:

$$\xi_c = \left(\frac{CT}{CT + e^{-BT}} \right),$$

where C = 1×10^{-9} and B = 0.0525 with T is in Kelvin. The experimental data are compared to the model with these parameters in Figure 22. In the simulations shown in the upcoming sections, we have simplified this to be a constant value, which means that the viscosity fit is probably worse than that shown in Figure 21. For future work, we hope to add this option to the computational model.

.

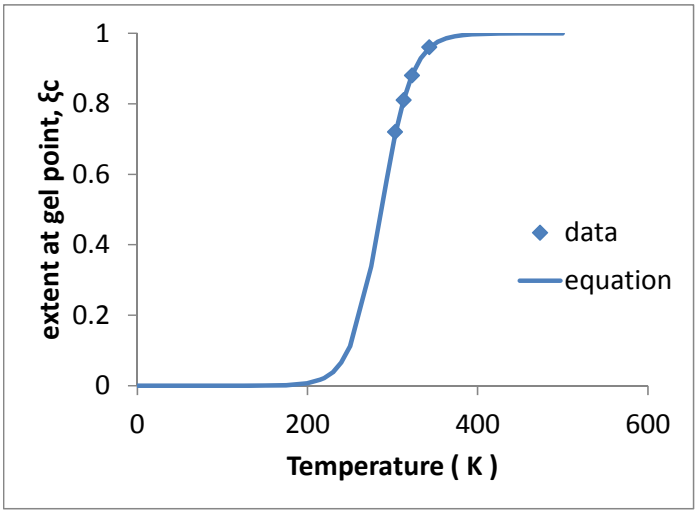

Figure 22. Fit for the critical extent of reaction at the gel point.

3.5 Foaming Material Viscosity

3.5.1 Steady Shear Viscosity

The foaming material does not follow the Cox-Merz rule; therefore, we test its rheology using steady shear in a parallel plate geometry. Earlier tests on the 44307 PMDI-4 encapsulation foam showed that polyurethane foam is very shear thinning, presumably due in large part to bubble breakage at higher shear rates [Mondy et al. 2013a]. For the structural BKC 44306 PMDI-10 foam it was confirmed that the measured shear viscosity was independent of shear rate at 0.01 s^{-1} and below. A study varying the gap between the plates (0.5 mm to 2 mm) showed that there was a small effect on the measured viscosity, but this effect was small compared to the change in viscosity with time, so no attempt was made to correct the data for slip. The viscosity changes about 5 orders of magnitude during the foam expansion; therefore, even a three-fold uncertainty in the absolute value is small compared to the effect of cure and gas fraction. Measurements were taken (at 0.01 s^{-1} and with a gap of 1 mm) at five temperatures from 30 to 70°C in increments of 10°C. Measurements were taken until the data became inconsistent around a viscosity of about 1×10^{7} Pa s, which we presume is near vitrification, and is several minutes after

the foam has stopped expanding. For example, at 30°C the foam stops expanding about 5 minutes after mixing the two parts, and at 50°C it stops after about 2.5 minutes.

The Taylor-Mooney equation (17) is thought to be valid for emulsions up to a discrete-phase volume fraction of about 0.5. We tested this form by using the model results of the previous subsection for the continuous phase viscosity as it changes with time combined with the predicted gas fraction derived with the model presented in the previous section. The foaming rheology and the full rheological model including the Taylor-Mooney terms are shown in Figure 23. At early times, when the bubble volume fraction is less than 50%, the method works fairly well as seen observed previously [Mondy et al., 2014]. However, at later times and higher bubble fractions, the Taylor-Mooney relation over-predicts the foam viscosity.

Because the model is not yet predictive and the high values of the viscosity can wreak havoc with our simulations, we have been using the curing viscosity only and ignoring the bubble-dependent terms. At the early times we are interested in for foam filling, this is probably a good assumption. This is especially so, because the wall tends to repel bubbles and see the continuous phase more clearly, except in very small sections of the mold. However, in future work, we would like to have a more predictive viscosity model.

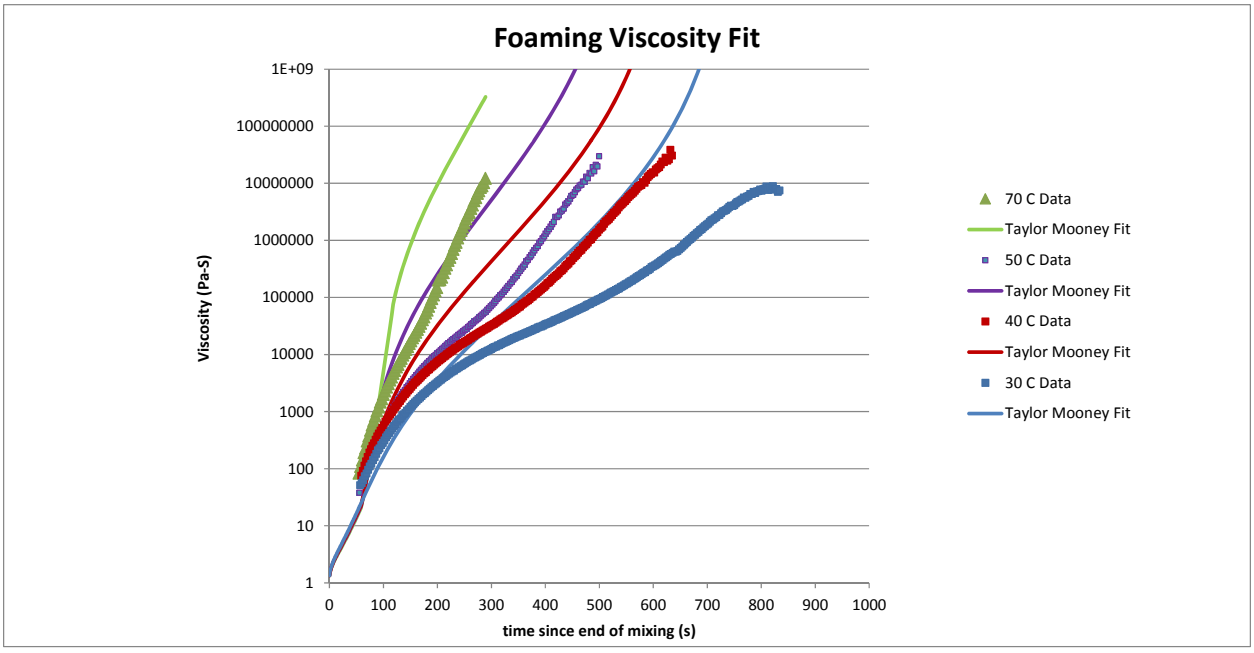

Figure 23. Foaming rheological data compared to combined Taylor-Mooney with polymer curing viscosity model

3.6 Thermal Properties

Thermal properties are important to predictive modeling of foaming processes since the foams react exothermically, producing energy, and to an evolving thermal environment including

variable for mixing, curing, and post-cure solidification. The main thermal properties for the model are heat capacity, thermal conductivity, heat of reaction, and density.

3.6.1 Heat Capacity

Measurements of thermal diffusivity were taken with a Hot Disk® sensor (Thermtest Inc., Fredericton, NB, Canada) on cured BKC 44306 PMDI-10 foam samples, blown and cured according to the KCP protocol. Here, the sensor was sandwiched between two halves of the sample. Unfortunately, the data for BKC 44306 PMDI foam (Figure 24) appear to depend on the density of the foam. This is in contrast to similar measurements made on the encapsulation polyurethane foam BKC 44307 PMDI, which showed little if any dependence on density, although the scatter encompassed almost the range of values in the structural data. At the present time this apparently strong density effect is unexplained. Results are compared with equation (20) in Figure 24, where $C_{p,liq}$ is taken as a polynomial fit to DSC data at temperatures from 0 to 160°C [Mondy et al. 2014]:

$$C_{p,liq} = 2.49x10^{-7}T^3 - 2.48x10^{-4}T^2 + 8.89x10^{-2}T - 9.85 \qquad (23)$$

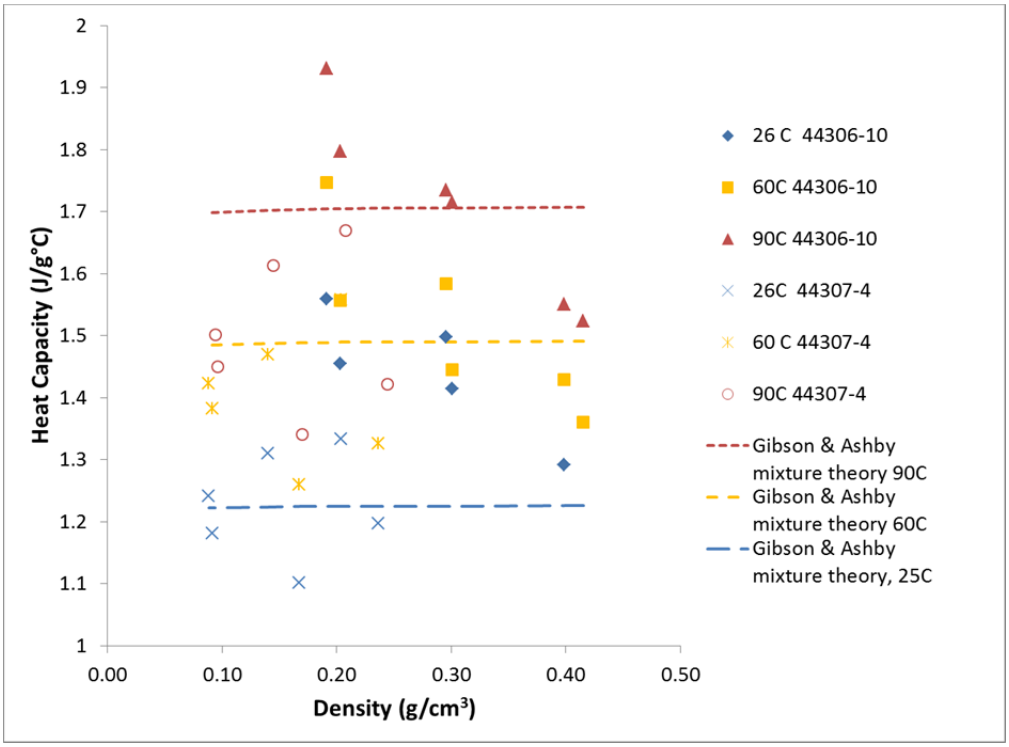

Figure 24. Measured heat capacity per unit mass of two types of PMDI foam molded to several densities. Dotted lines are the results of equation 20 [Gibson and Ashby 1990] combined with DSC measurements as the value for the continuous phase.

3.6.2 Thermal Conductivity

Thermal conductivity measurements were made on the same cured foam samples as used in the previous subsection. Figure 25 shows the thermal conductivity as a function of temperature for a non-foaming sample. For each test a value is obtained for the upper layer (red) and the lower layer (blue). These results could potentially be used to approximate k_{liq}. Because it is impossible to make a sample completely free of bubbles, we estimate the value of k_{liq} by extrapolating the full set of data to the original liquid density (1.18 g/cm^3).

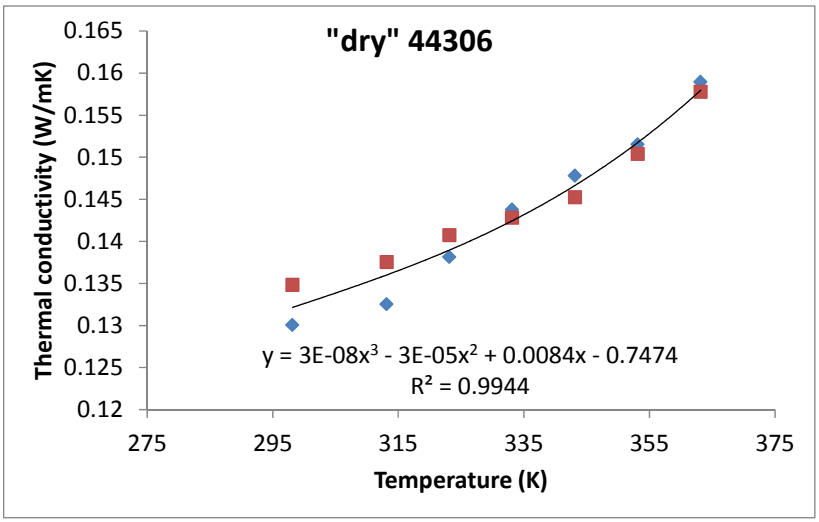

Figure 25. Thermal conductivity for a cured sample made from dried material that does not foam.

Experimental results for thermal conductivity of the foam as a function of density are shown in Figure 26 and compared to predictions from equation (24).

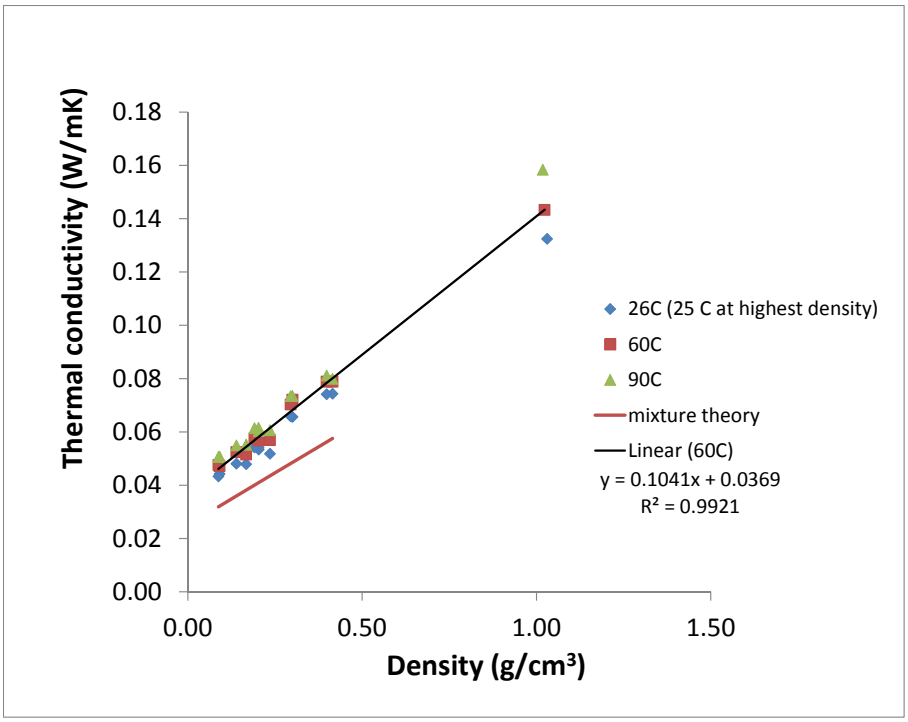

Figure 26. Thermal conductivity at three temperatures for several densities of foam. The red line shows results of equation 21 for the thermal conductivity at 60°C, using the polynomial fit in Figure 25 as the value of k_{liq}. T.

The values for the mixture theory appear to trend with density in approximately the correct way; however, these under-predict thermal conductivity compared to the measured data. New measurements are available, which actually trend better with mixture theory and show a lower average thermal conductivity than our measurements [Phinney, 2015].

Table 6. Thermal Properties Used in the Simulations

Thermal Properties	Value
Heat capacity gas $C_{p,gas}$	2.0 J/g K
Heat capacity, liquid, $C_{p,liq}$	1.0 J/g K
Thermal conductivity gas, k_{gas}	0.025 J/m K s
Thermal conductivity liquid, k_{liq}	0.180 J/m K s
Heat of reaction, ΔH_{rxn}	181 J/g

3.7 Density Variations

One goal of this work is to provide data to validate an improved model that can better predict density variations in the final structural foam part. To this end we have measured the density with height of several of the bars molded in the volume-*vs.*-time experiments. With the simple

bar geometry we can cut the bar into pieces, measure, and weigh them to obtain densities within a section of the bar. We can also use X-ray computed tomography (CT) to determine the spatial density variations.

3.7.1 Bar Geometry

Three subsections approximately 0.25 cm in length were cut from representative bars. The length of a bar made in this mold is 7 3/8 inches (18.73 cm), but most free-rise experiments result in shorter bars. The foam made at 30°C was very fragile and the samples in the center region crumbled before density could be measured. Individual sample density measurements are compared to the overall bar density determined from image processing the final frames in the volume-*vs.*-time experiments (Figure 27), showing that the overall density is a function of the mold temperature during the foam expansion. The spread in the data is a consequence of the density variation along the length of the bar, as shown in Figure 28. In all cases the density is highest near the bottom of the bar and lowest near the top, consistent with possible "creaming" of the lighter material to the top and draining of liquid to the bottom, but opposite of what has been observed with lower density encapsulation foams.

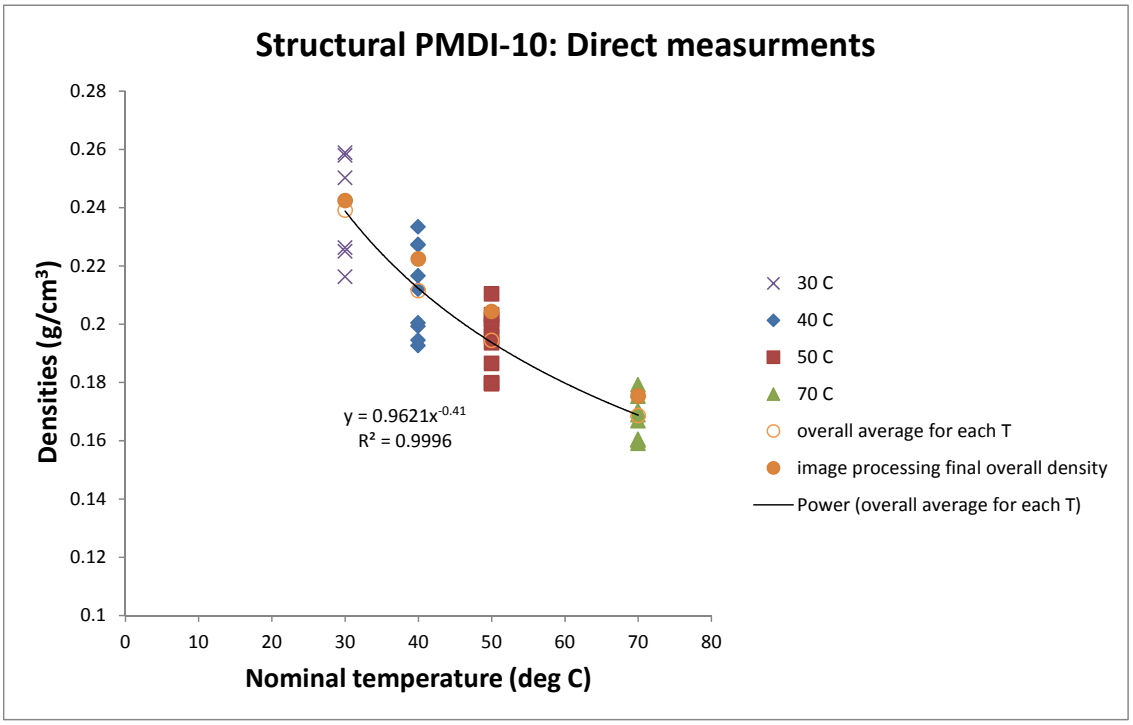

Figure 27. Densities measured from image processing video frames at the end of foam expansion and from cutting representative samples at several locations (three replicas at each location).

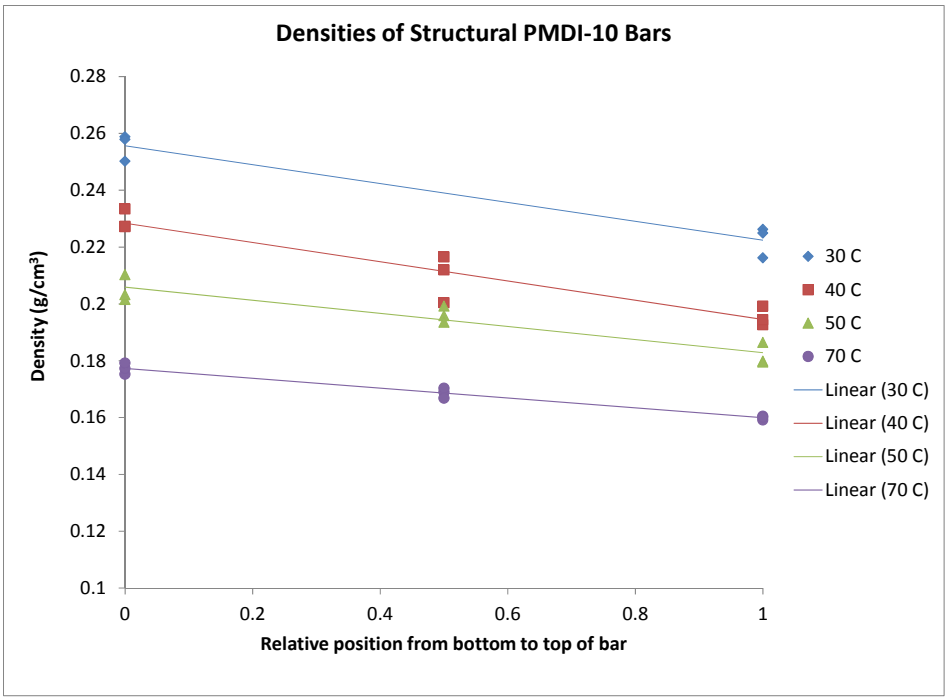

Figure 28. Densities of samples taken at three different locations and measured by weight for four different temperatures. Lines are to guide the eye.

X-ray CT was also performed on representative bars. An X-ray image from this work is shown in Figure 29, where samples 1 and 2 are the same free-rise BKC44306 PMDI-10 foam samples molded at 30 and 50°C, respectively, as in the previous figure. Sample 3 is the same foam molded at 30 °C but over-packed to a nominal density of 0.32 g/cm^3 (20 lb/ft^3), although some leakage occurred leading to a slightly lower density. All samples contain fairly large voids as can be seen by the dark patches.

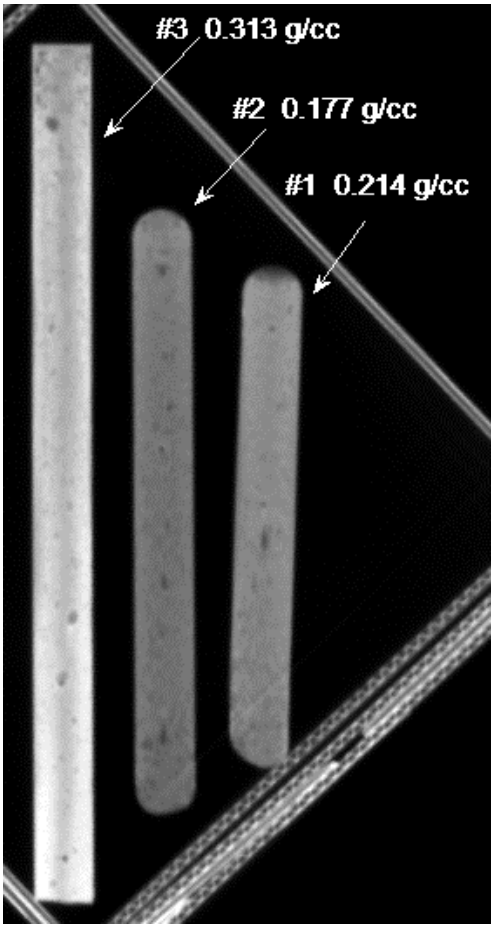

Figure 29. X-ray image of several bars of BKC 44306 PMDI-10 foam. 1)Sample 1 is free rise at 30°C, 2) Sample 2 free rise at 50°C, 3) Sample 3 is 1.5 times over packed at 30°C.

Four samples of foams were molded to different densities, cut and weighed, for use as calibration objects. The profiles of intensities measured in the bars show variations from the arrangement of larger bubbles. This is shown for samples 1 and 3 in Figure 30 and Figure 31, respectively. The X-ray data seem to be consistently lower than the image processing or direct weight measurements, although much more subtle variations can be seen by using the X-ray CT technique.

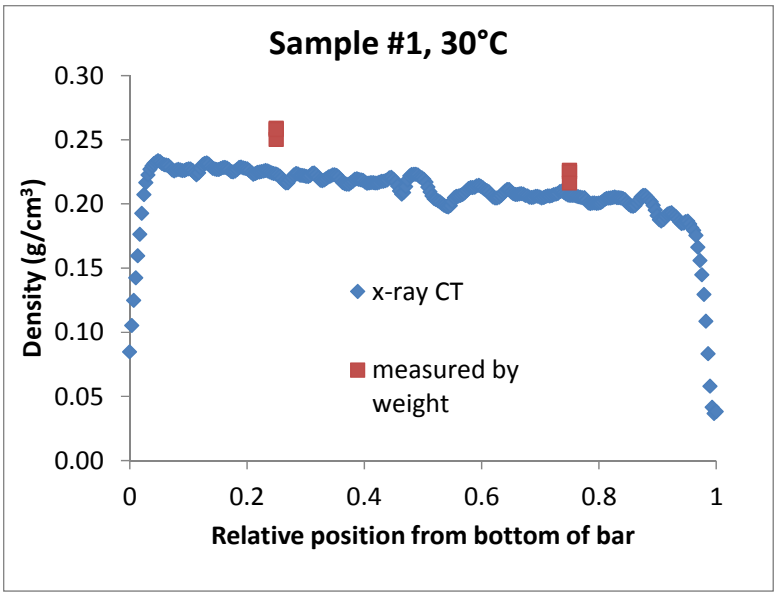

Figure 30. X-ray CT measurements of density profiles compared to the direct weight of samples cut from sections of the bar for free rise foam at 30°C (sample 1).

Sample 3 exhibits the same trend in density from highest at the bottom to lowest at the top, even though the foam was double packed (Figure 31). The slope is more pronounced for the over packed foam.

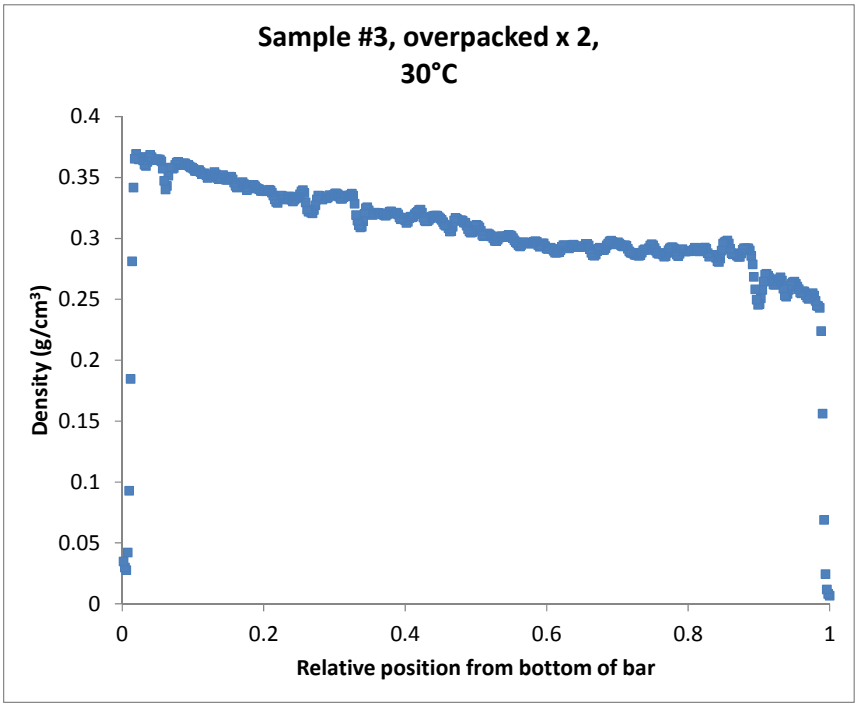

Figure 31. X-ray measurements of density profile in a bar packed to double density.

4. NUMERICAL METHOD

The equations of motion were discretized with a stabilized finite element method. An Eulerian level set method was used to track the location of the free surface between the foam and gas as a function of time [Sethian, 1999]. The method is very similar to our previous work, except property averaging is used instead of equations averaging to handle the change in properties from the foam to the gas phase.

The level set, ϕ, is a signed distance function with the level set zero demarcating the foam-gas interface. We advect the level set with the fluid velocity, to update the interface position with time. Because this is a kinematic equation, it is only true at the foam-gas interface. Elsewhere, the velocity field distorts the distance function, which must be redistanced periodically to make it a distance function again. A constrained Huygens redistancing is used to reduce mass loss during this step [Rao et al., 2012]. The level set equation is hyperbolic and must be stabilized with upwinding.

$$\frac{\partial \phi}{\partial t} + v \cdot \nabla \phi = 0 \tag{25}$$

Properties depend on level set in the equations of motion:

$$\begin{aligned} &\rho(\phi)(\frac{\partial v}{\partial t} + v \bullet \nabla v) = -\nabla P + \nabla \cdot (\eta(\phi)\dot{\gamma}) + \rho(\phi) g \\ &\frac{d}{dt}\rho(\phi) v = 0 \end{aligned} \tag{26}$$

A numerical Heaviside function, *H(ϕ),* modulates the properties from foam to gas for viscosity and density. Surface tension is applied at the interface and gravity is important force in the problem.

$$\begin{aligned} \eta(\phi) &= (\eta_{gas} - \eta_{foam}) H(\phi) + \eta_{foam} \\ \rho(\phi) &= (\rho_{gas} - \rho_{foam}) H(\phi) + \rho_{foam} \end{aligned} \tag{27}$$

Dohrmann-Bochev pressure stabilization is used to both reduce the condition number of the matrix and allow for equal order interpolation [Dohrmann and Bochev, 2004]. This also enables the use of Krylov-based iterative solvers available through Trilinos [2015]. We segregate the solution at each time step in three different matrix systems with only loose coupling: we first solve the level set, then momentum and continuity, and then the species and energy equation. The method implemented in Sierra Mechanics Aria [Notz et al., 2007]. Further details of the modeling approach and equations, the numerical methods used and the finite element implementation can be found in a paper by Rao et al. [2012].

Boundary conditions for foams are complex, because foam slip at the walls. We implement this using a Navier slip conditions [Bird et al, 1960], that is applied to the momentum equation.

Because this is dependent on the stress, a phase-dependent slip velocity must be used where β must be much greater for the gas phase than the foam phase.

The phase dependent slip takes the form:

$$n \cdot \underline{\underline{\tau}} \cdot n = \frac{1}{\beta}(v - v_s) \cdot n \tag{28}$$

$$\beta = (\beta_{gas} - \beta_{foam})H(\phi) + \beta_{foam} \tag{29}$$

Where n is the normal to the solid surface, v_s is the velocity of the solid surface, usually zero for our applications. The slip in the gas coefficient, β_{gas}, is usually assumed to be 200 times the slip coefficient in the foam phase, β_{foam}, to allow for more physically realistic gas behavior. Without this modification, the gas moves too slowly and refuses to leave the mold, which is contrary to what is observed in experimental foam filling applications.

Vent boundary conditions can be complicated as well, since under real foaming conditions the foam closes off the vents that the gas could easily escape from. We represent this self-closing venting behavior by using a similar phase dependent boundary condition.

$$n \cdot \tau \cdot t = \frac{1}{\gamma}(v - v_s) \cdot t \tag{30}$$

$$\gamma = (\gamma_{gas} - \gamma_{foam})H(\phi) + \gamma_{foam} \tag{31}$$

Judicious choice of γ allows the gas to escape unfettered and then creates a no penetration boundary for the foam.

For the energy equation, Dirichlet boundary conditions are used to represent the preheating of the mold to a temperature of 40°C. The heat transfer in the mold is not included in the model. Initial conditions include setting the temperatue of the foam to the processing temperature, 30°C, and setting the initial water and carbon dioxide concentration from the foam formulation. The intial weight of the foam and location of the foam-gas interface is inferred from the experiment.

5. MODELING RESULTS

We exercise our newly developed foam filling and curing model on several geometries similar to encapsulation and structural foams molds used at Sandia National Laboratories. These are geometries that are simplified version of real parts, but suitable for unlimited release. The first geometry we examine is called the Mock AFS, which is a clear mold similar to the multi-board structure of an AFS but flat and without any components. The second geometry we examine is similar to a structural part. For this, we have a made a clear mold and designed two different filling configurations: (1) a bottom up filled termed “Pie Mold, ” (2) a dual fill approach called the “Cake Mold,” where the part is filled upside down from the pie configuration with foam

dripping down from the top and foaming up from the bottom. The "Cake Mold" configuration was chosen based on information about how the structural parts have been filled in practice. Modeling results are compared to the closest available experiment, though some comparisons are only qualitative because a different foaming system was used. Finally, we examine the bar geometry discussed in section 3.7.1 and compare the results predicted from the model for final part density to the X-ray CT-data.

5.1 Mock AFS

The Mock AFS is an idealized foam encapsulation part, with three flat plates in a cylindrical mold. For the real part, the plates would be covered by small electronic parts and the foam would need to infiltrate the interstitial spaces between these small features. The dynamics of the filling process is quite complex, and is a complex function of temperature, gas generation, curing, and viscosity evolution. The experimental flow visualization results are shown in Figure 32, giving three different camera views. The front is shown on the left, the side view in the middle, and the back view is on the right. Nine different time planes are shown. The foam used here is the encapsulation foam with water content for a 4lb/ft^3 free rise foam. Excess material must be used in order to fill the entire mold since so much foam is lost through the center vent before the side plates fill completely with foam.

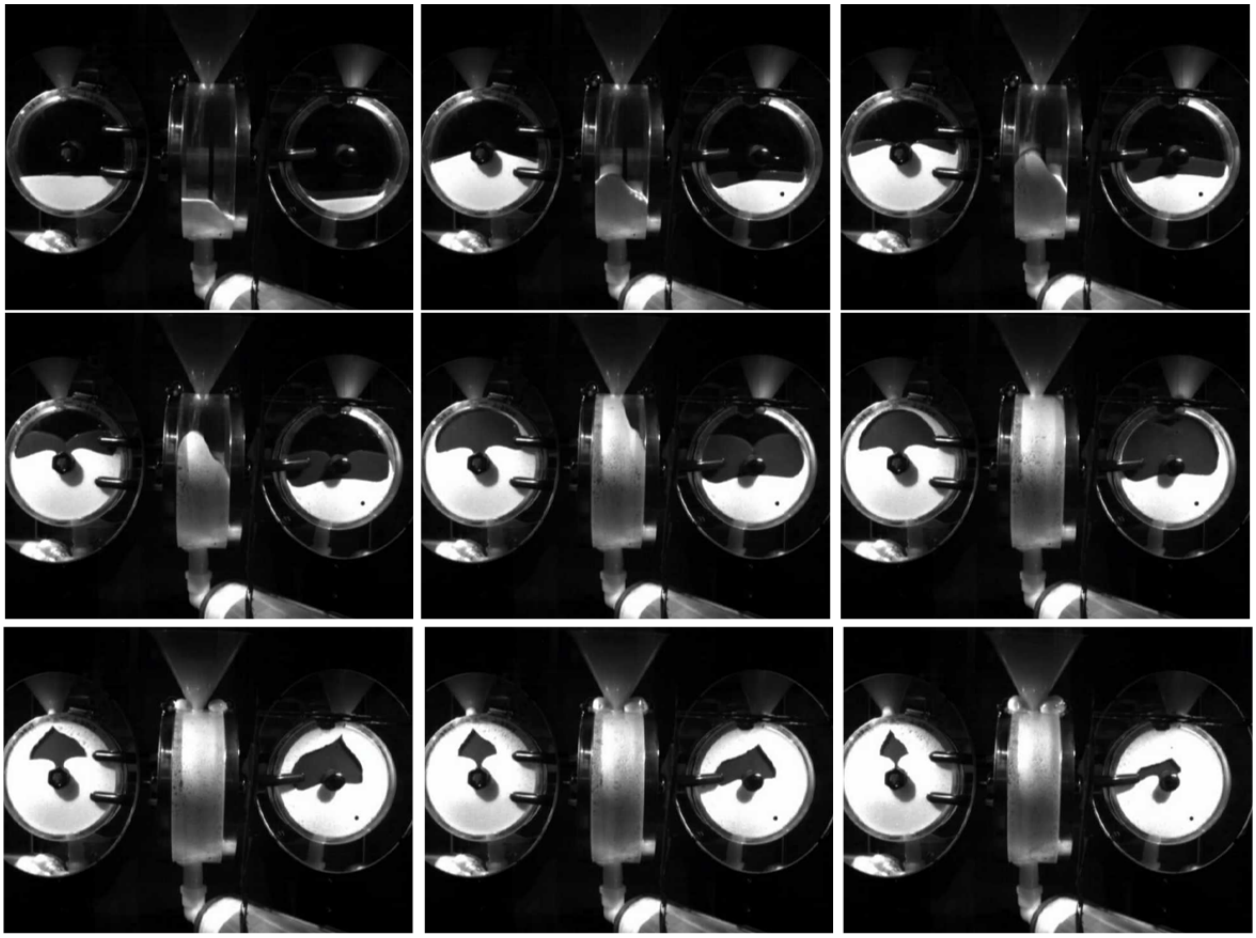

Figure 32. Mock encapsulation experiment with encapsulation foam. Time increases from left to right and then down, e.g. the initial condition is on the left-top of the 3 by 3 grid and the final filling profile is on the bottom-right of the grid.

The mesh for the Mock AFS is shown in Figure 33, where the foam comes in though the entrance gate shown on the left and is vented at the three vents on the right of the figure. Filling actually occurs in the vertical direction. The foam must fill in the regions between the three unequally spaced plates.

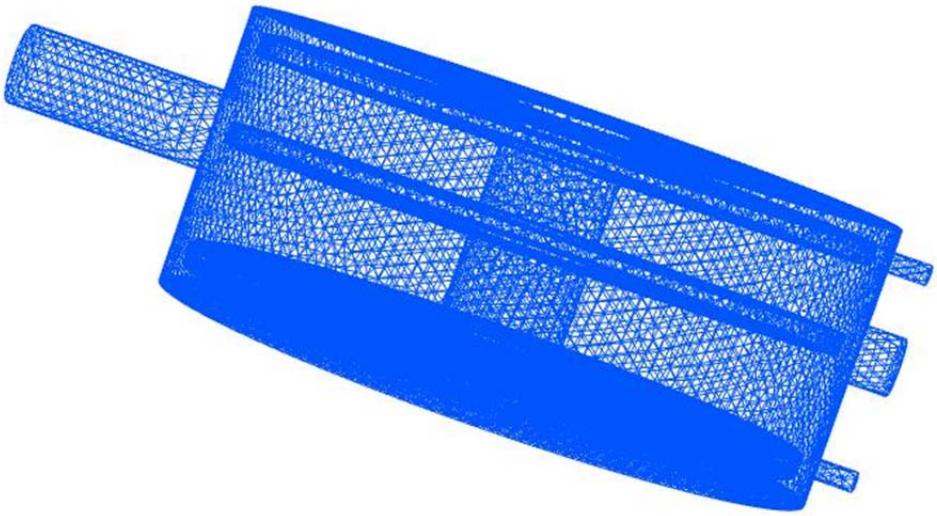

Figure 33. Mesh for mock AFS simulations

For this simulation, we were trying to compare our predictions to the only experiments currently available in this geometry, which were for an encapsulation foam that has slower curing chemistry and has a higher water content to reach a lower final density of 4lb/ft^3. The encapsulation foam is processed at 70^{o}C while the structural foam is processed at 30^{o}C. For these different temperatures, the foaming dynamics take place over a similar time frame of foaming in 150s - 300s for the encapsulation and structural foams.

For the simulation, the mold is preheated to 40^{o}C and the foam comes in at 30^{o}C. The inflow is asymmetric and fills thinner area first. Our mesh is slightly more symmetric than the experiment, so we capture this effect by slanting the initial front location toward the thin plate. The foam slips at the wall using a Navier slip condition with β_{foam} =0.001 and the gas slips ten times more than the foam, β_{gas} = 0.01. Using a small amount of slip for the foam and a slightly larger amount for the gas was important for matching the dynamics of the real filling process. Results for the filling of the "Mock AFS" with structural foam are shown in Figure 34.

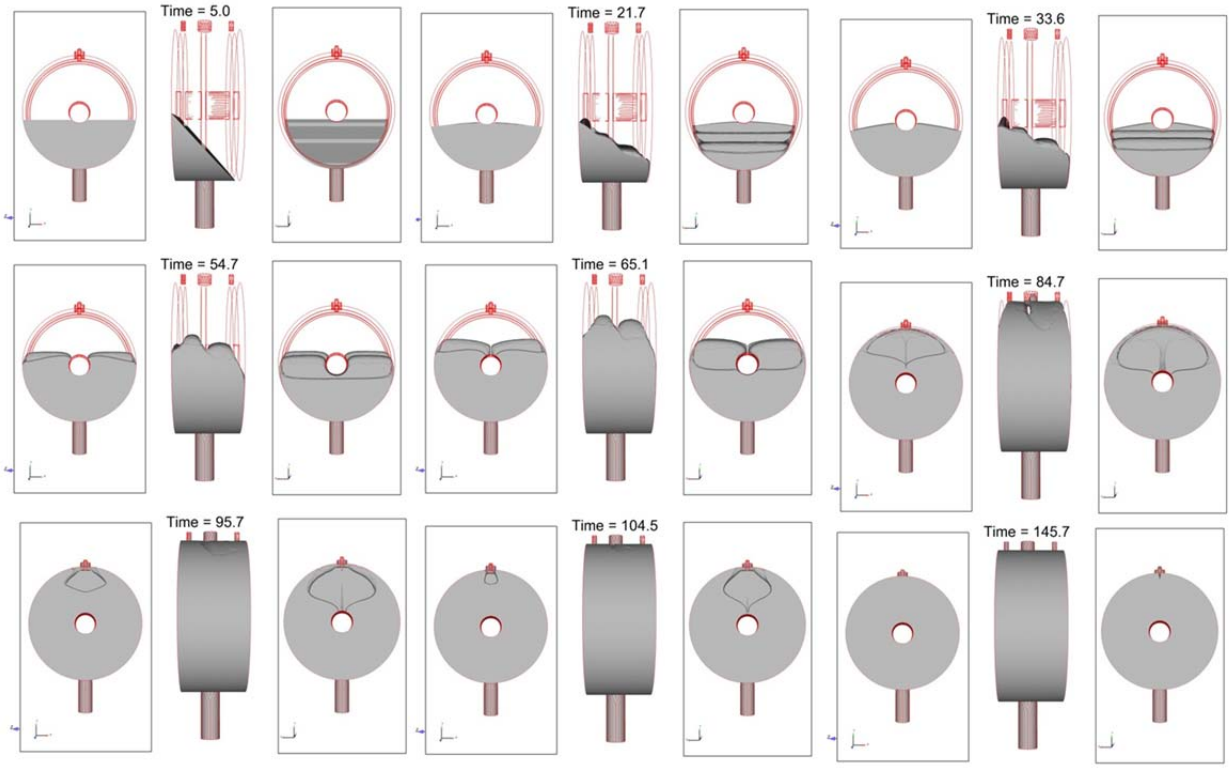

Figure 34. Mock electronic encapsulation using structural foam model. The frames are organized in a 3 by 3 grid similar to the experimental results in the previous figure.

The foam enters the mold and is skewed toward the left side of the mold because of the asymmetry of the gate. Over time, the interface flattens but the left edge is still fuller than the rest of the mold, as seen by the second time plane. By the fourth time plane, the center channels begin to fill faster than the sides due to the effect of drag on the walls. The center continues to fill faster than the thinner side channels. At t=95.7s, the center channel foam has reached the central vent while large voids still occur in both the side plates. The material is allowed to leave via the central vent in a manner similar to the experiment. After t=145.7s all voids have been filled and the material has reached both the other vents.

Note, that we could not capture this complex interplay of nonlinear effects with our previous model where density was prescribed [Rao et al., 2012], but the newly developed model matches the experiments quite well.

5.2 Mock structural parts

Two methods were investigated to fill a mock structural part (Figure 35), which was designed to have the features similar to real parts with cut outs and larger sections but to be a simpler geometry to allow manufacturability in a clear mold suitable for flow visualization. The first filling orientation we call the “Pie Mold” where material fills from the bottom with the mold in an upside configuration from Figure 35. The other filling method we call the “Cake Mold.” This is a more complex filling profile which is in the orientation of Figure 35 but with foam pouring down from the top and foaming up from the bottom.

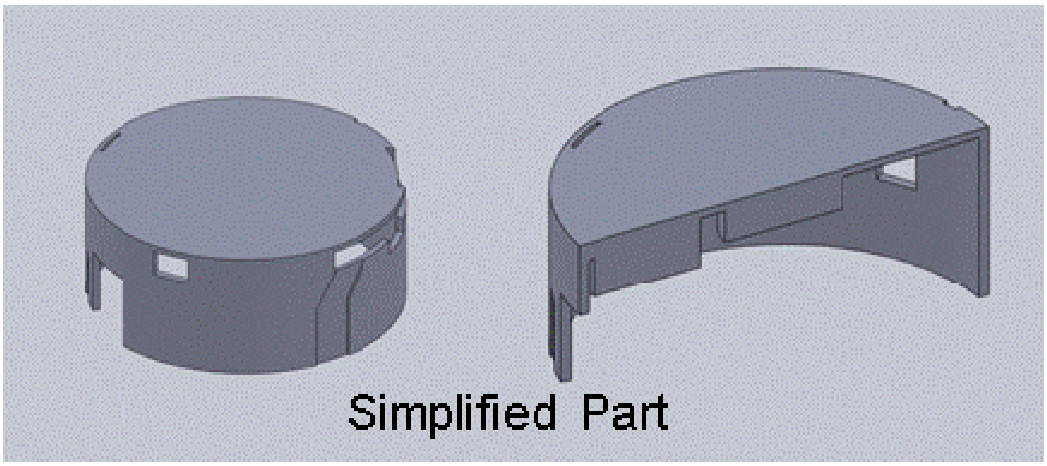

Figure 35. Image of simplified part to be filled in two orientations.

An image of the part foaming in the oven is given in Figure 36 for the "Cake mold." The oven is instrumented to give four camera views and has multiple temperature sensors.

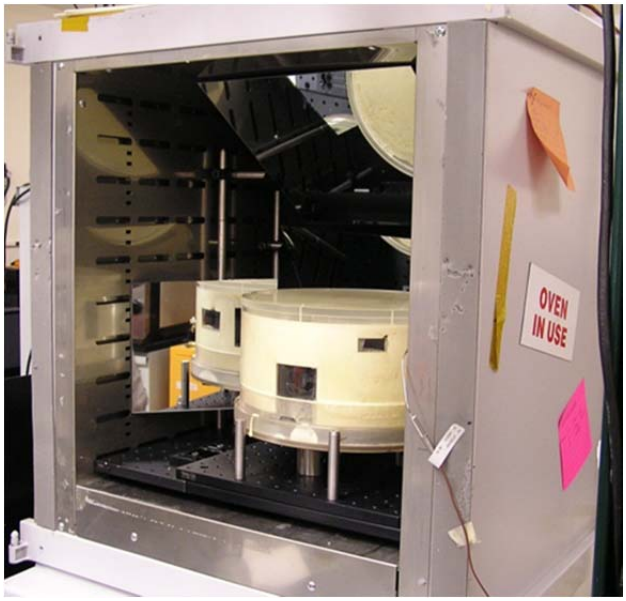

Figure 36. Cake mold filling process curing in the temperature-controlled oven.

5.2.1 Pie Mold

The "Pie Mold" used 10 lb/ft^3 free rise structural PMDI foam, slightly over-packed to produce a 13 lb/ft^3 part. To ease processing and slow the foaming and curing reactions, no preheats were used. The foam was mixed for 30s instead of 60s, also to allow more time to pour the fast-reacting material. Once mixed, the foam was poured into the reservoir which was the lid of the upside down part. The reservoir is a clear plastic cylinder without features. The insert has a complex cylindrical shape and contains three-dimensional features. After the foam is poured into

the bottom of the cylinder, the insert was pushed into the reservoir. The geometry of the insert is shown in Figure 37.

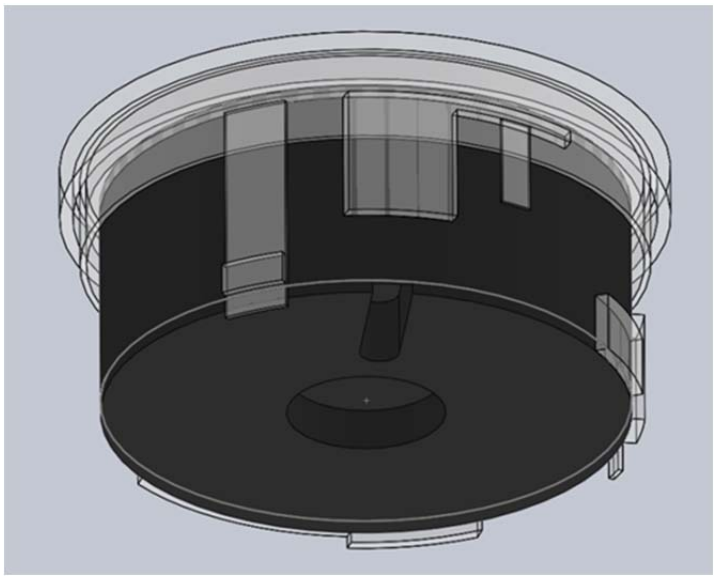

Figure 37. Insert pushed inside of the mold down into bowl that once was the lid.

Flow visualization results from the filling process are shown in Figure 38. The experiment resulted in a short shot showing the last places to fill. The polymerization reaction vitrified before the foam could complete filling the mold. This was an early experiment with the structural foam where we were still working to understand the pot life and processing window. The encapsulation foam, which we had more experience with, has a much longer pot life.

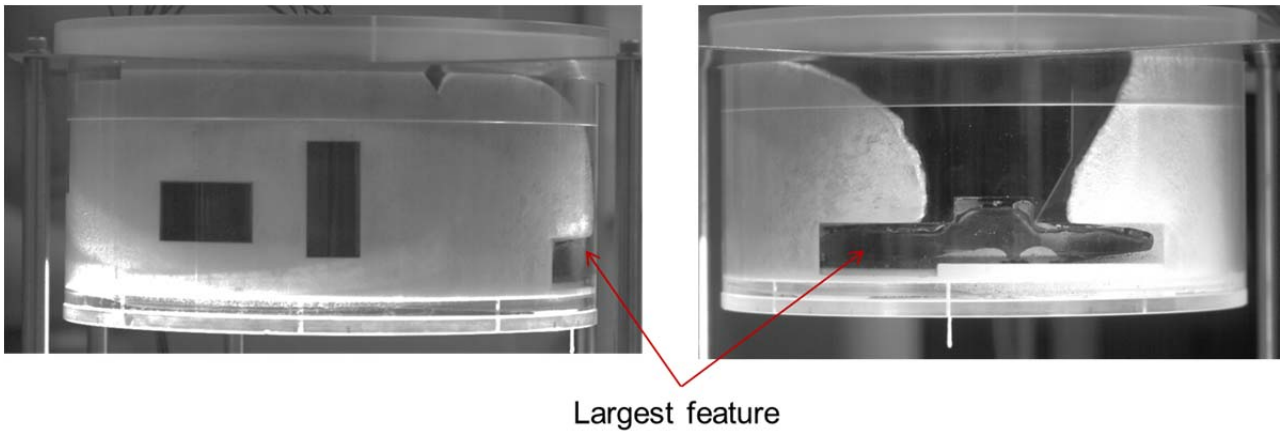

Figure 38. Flow visualization of the foaming process for the "Pie Mold." The experiment resulted in a short shot showing the last places to fill. The polymerization reaction vitrified before the foam could complete filling the mold.

Once the "Pie Mold" was filled, X-ray CT was used to determine void locations in areas that could not be inspected visually. The results are shown in Figure 39. From this data, we can see

that large pockets of trapped gas are found under the two large features in the bottom of the mold.

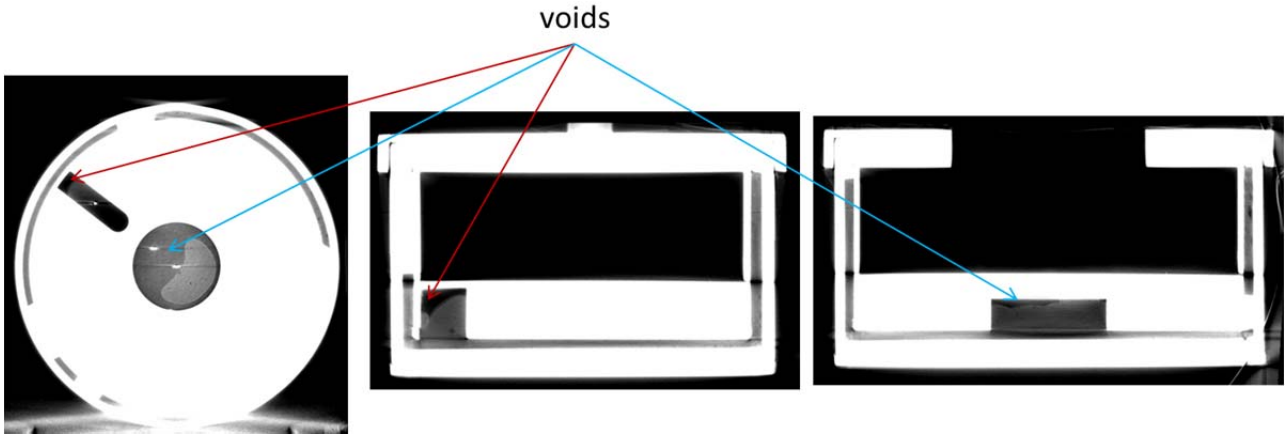

Figure 39. X-ray CT of "Pie Mold" shows that the large features are left with voids, large regions of trapped gas

We ran a similar scenario of a "Pie Mold" filling using Sierra Aria and our foam filling model. Figure 40 shows the finite element geometry and vent locations for the simulation. Vents are placed on the two large features and also around the top of the mold. These vents are larger than those used in the real system, but placed in similar locations. Our gas model retains too much gas compared to the experiments. Enlarging the vents has been shown to match the data better and give more physically realistic gas dynamics.

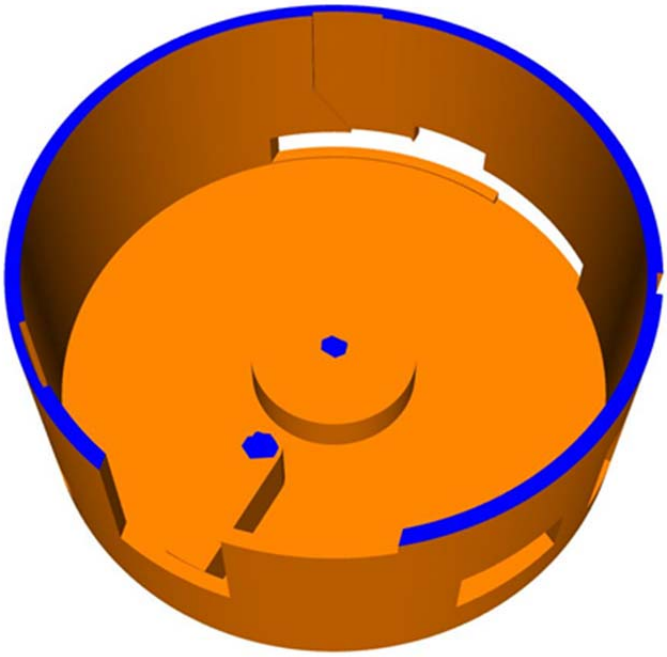

Figure 40. Vents and geometry for "Pie Mold" geometry. The vents are shown in blue.

The filling profiles for this geometry are given in Figure 42. We start out with a uniform fill at the bottom, and ignore the punching down of the insert. The foam slowly fills up the sides of the mold, creating knit lines above the large feature similar to what is seen in the experiment. For the simulation, we can see the mold eventually fills completely, probably because more material was added to the simulation than was actually available to fill the real mold. Air is trapped underneath the two features in the bottom of the mold. Similar results were seen in X-ray analysis of the experimental part.

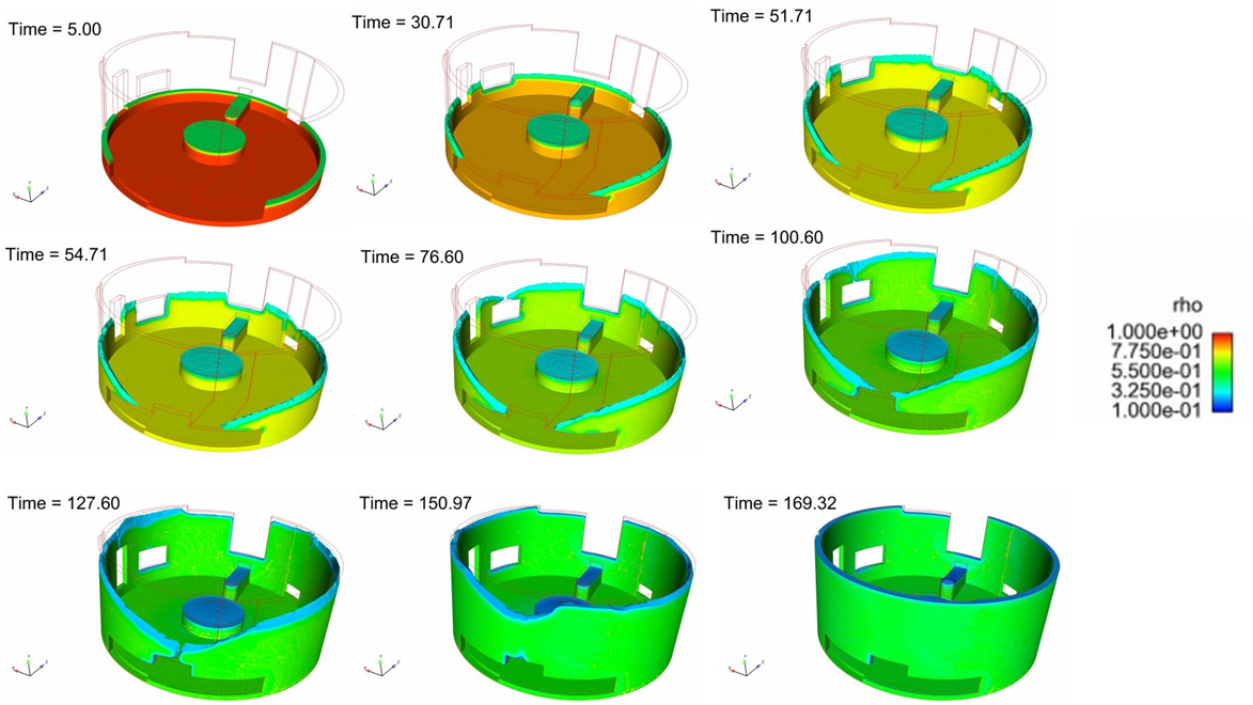

Figure 41. Density and filling location for structural foam in "Pie Mold."

The model calculates the molar volume of carbon dioxide and uses that to predict the final density of the part. These results can be seen in Figure 42. The concentration of carbon dioxide is highest under the large circular feature and lower on the walls. The concentration is very noisy, possibly due to numerical oscillations. We are still trying to determine the cause of the noise, since the advection-diffusion-reaction equations are treated with either Taylor-Galerkin or streamline upwind Petrov-Galerkin [Hughes, 2006]. The density varies with the lowest density seen at the bottom and trapped gas below the large features. The density is higher at the walls than in the interior of the mold. The model predicts a thin skin of lower density at the walls, mostly due to temperature gradients.

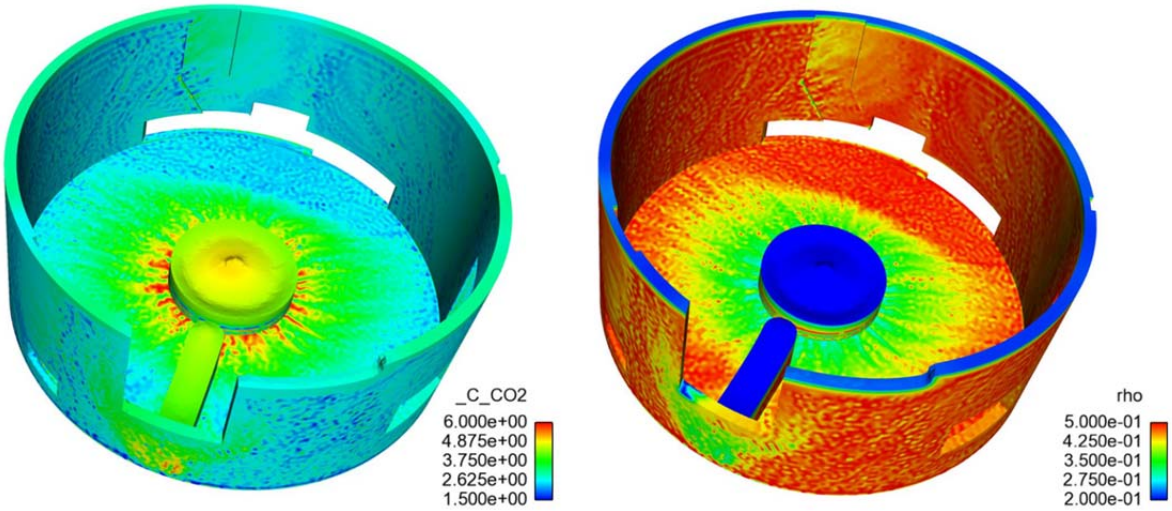

Figure 42. Carbon dioxide concentration (.01 scaling of mmol/ml) and resulting density variations (g/cm^3) in pie mold showing voids under large features.

5.2.2 Cake Mold

The "Cake Mold" was also filled in a more traditional way with a dual pour, as was used historically for structural molds at the Kansas City Plant. The geometry is shown in Figure 43.

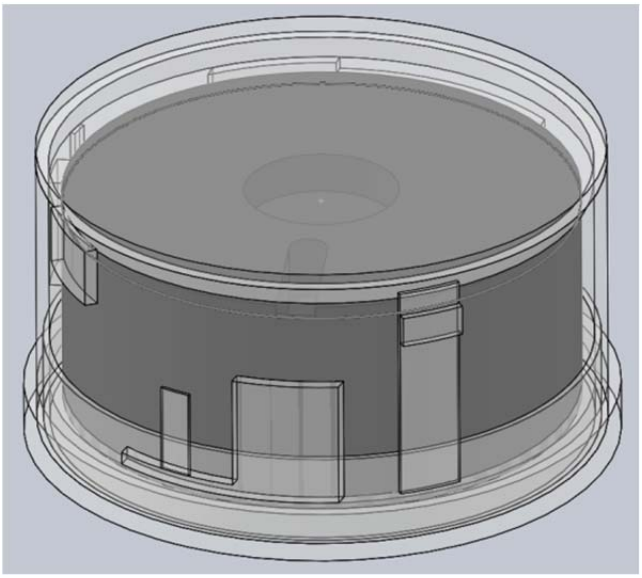

Figure 43. "Cake Mold" configuration of mock structural mold

Because this was our first effort to design an experiment with a structural mold, we began by using the slower reacting encapsulation foam, which is more forgiving to work with. We used 10 lb/ft^3 free rise encapsulation PMDI foam at a quantity to produce a 14 lb/ft^3 part. The mold was preheated to 65^{o}C. The foam was mixed at room temperature without any preheats, which is typical for encapsulation foam kits. Foam precursor is added to the bottom reservoir in the mold and into the two large features, a rectangular and cylindrical reservoir, at the top of the mold.

Foam drips down from the top and foams up from the bottom, creating multiple knit lines as seen in Figure 44.

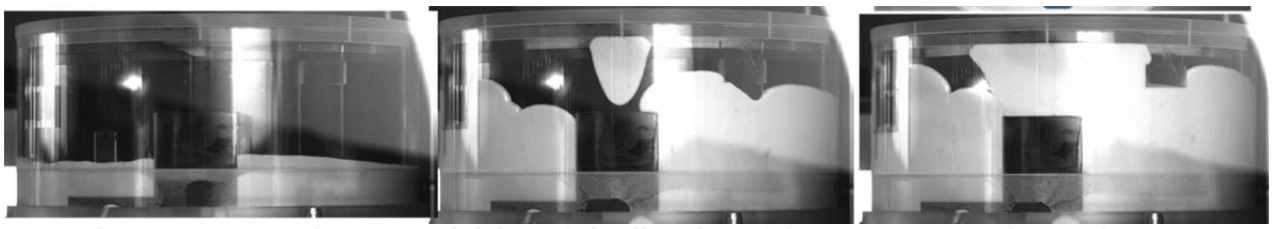

Figure 44. Foaming material is originally placed in top rectangular and cylindrical reservoirs and in the bottom rim reservoir, to simulate the legacy Kansas City foam pouring method.

The geometry is given in Figure 45, where a large number of vents are used to improve the filling process. Previous simulations with only the four vents on the top of the "Cake Mold" failed to fill. We place the vents along the sides of the "Cake Mold" where we think we will have issues with knit lines and trapped air.

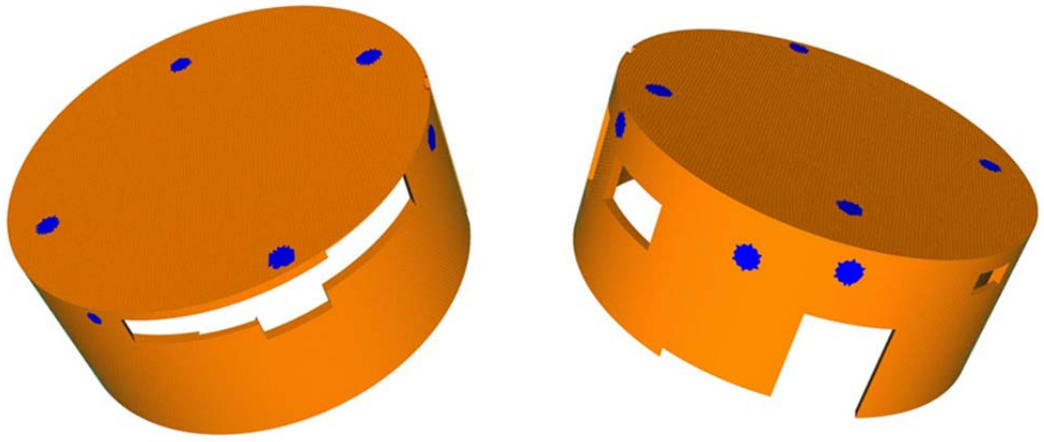

Figure 45. Mesh and vents for "Cake Mold." The vents are shown in blue.

The initial condition for the foaming process is similar to the experiment, though a larger amount of foam is added to the two top reservoirs because only simple initial conditions are available for initializing the level set. Results from the foaming simulation are shown in Figure 46. Again, we use the structural foam model and temperature to try to match an encapsulation foam experiment at 65^{o}C. Thus, the comparison is only qualitative.

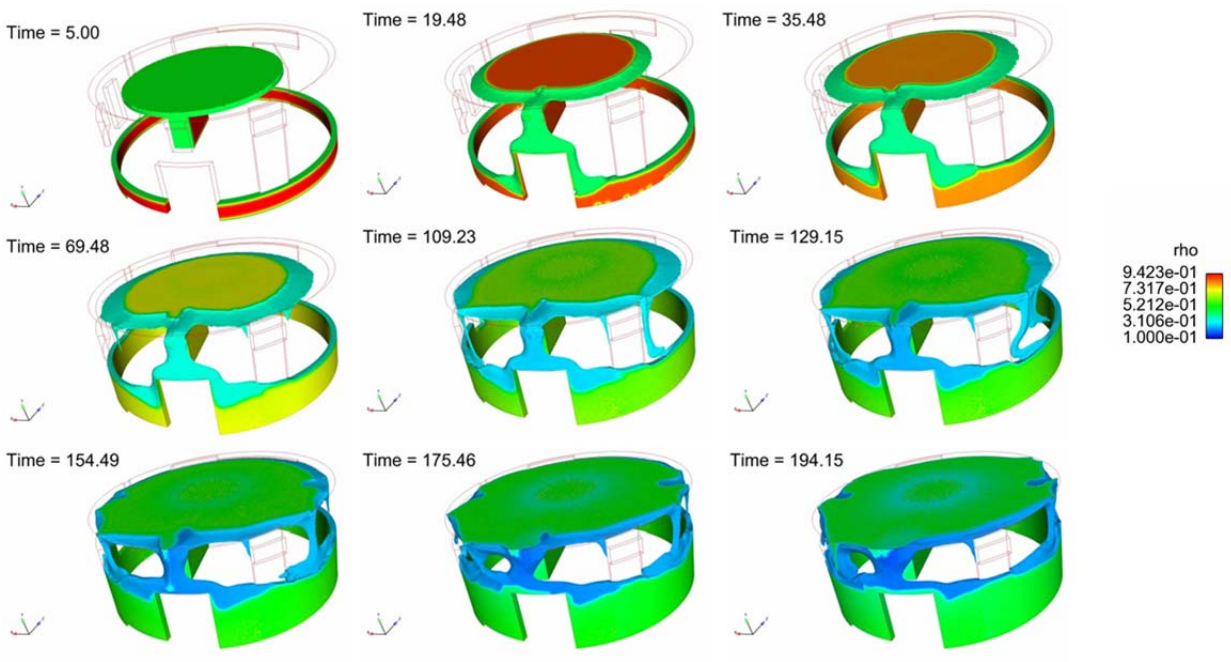

Figure 46. Simulations in the "Cake Mold" geometry

This simulation uses a nucleation time of 33s, so for the first two time planes the material foams little and mostly begins flowing down from the two top reservoirs. By the third time plane, foaming begins and the density starts to go down with the material expanding from both directions. By our final time plane at t=194s, we still have not filled the mold though filaments of foam have dripped down from the top reservoirs and the initial foam height of the bottom reservoir has more than tripled. We think that the reason for the poor numerical performance is the lack of mesh refinement. We have found that dripping simulations require meshes at least twice as fine as foaming simulations in order to capture the correct dynamics. This is especially true for thin walled structures like the cake mold. We are currently working on developing a more refined mesh. However, the qualitative behavior in the simulation matches experiment. The material drips down above the rectangular "window" and meets the foam rising from the bottom. The shapes of the predicted knit lines are approximately the same as observed in the experiment. The lack of symmetry in the experiment is most likely caused by uneven spreading of the material initially (left picture in Figure 44).

5.3 Density Predictions in Bar Geometry

Our model has been shown to be useful for predicting the dynamics of the filling process and the evolution of the free surface over time. However, we would also like to accurately predict the final density and density gradients as part of our "cradle-to-grave" modeling effort wherein we obtain material properties from filling simulations and use them to predict the structural response of the foam through manufacturing and then aging. The modulus of the nonlinear viscoelastic solid foam is very sensitive to the local density [Long et al., 2015].

To understand the accuracy of our density predictions, we began by studying a simple, well-controlled experiment, the bar geometry. Here we have data for filling times, mold temperature

and pressure and can post-test the resulting bars using X-ray CT as shown in section 3.7. The mesh for the bar geometry is shown in Figure 47, where the mesh is rotated horizontally to take up less space. The foam rises up from the bottom of the mold and the mold is placed vertically with gravity in the long direction.

Figure 47. Mesh for bar geometry density simulations. The mesh is fairly fine, so the mesh lines are hard to see.

A small amount of foam is added to the bottom of the bar mold, and then rises to produce a free rise foam with nominal density of 0.21 g/cc. The results for density are given in Figure 48 for the free-rise foam at 30°C. There is a small density variation, with the highest density found at the walls and the bottom of the container.

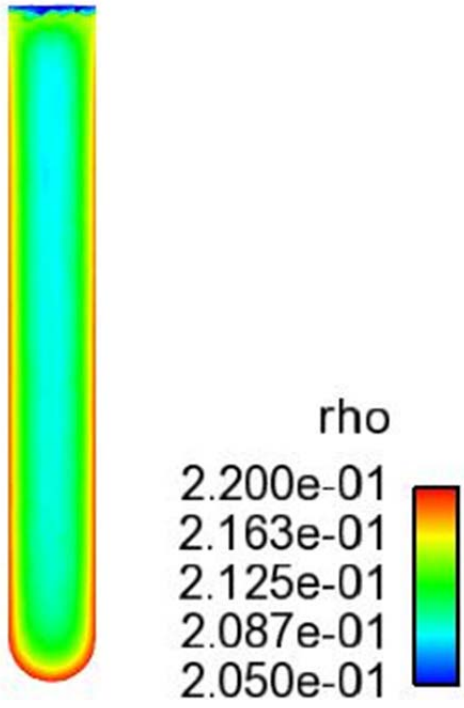

Figure 48. Free rise density predictions in bar geometry for PMDI-10 at 30°C.

The density variations are mostly driven by temperature. The temperature gradients and the maximum temperature with time are in Figure 49. The curing reaction causes an exotherm of 10°C, which is much higher than the temperature rise observed experimentally. This result

suggests that we need to carefully design a temperature validation study that focuses on the heat of reaction and thermal conductivity, as they are the most impactful parameters.

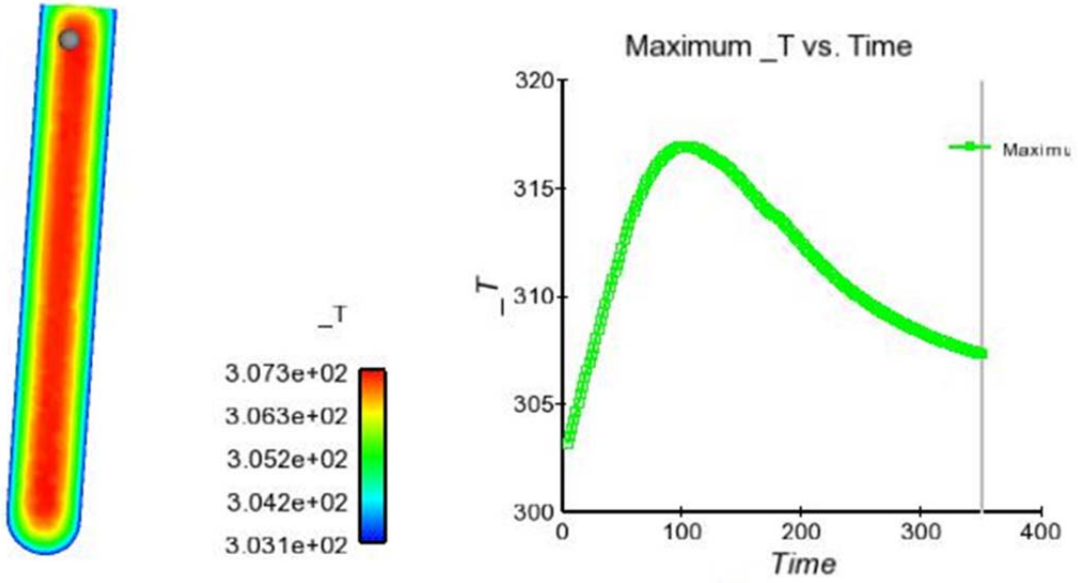

Figure 49. Exotherm causes 10°C temperature rise, which is higher than that seen in experiment. However, temperature gradients show that thermocouple placement is critical. Our thermocouple is placed in the center of the mold. A cooler temperature would be recorded nearer the wall.

Figure 50 compares the X-ray CT and measurements for density in the free rise foam at 30°C to the Sierra/Aria simulations. We have a compressible model that uses the ideal gas law for the gas behavior and allows some compressibility in the foam. Though the simulations capture the correct average density, the density gradients are much larger in the experiment than the simulations. This discrepancy may be due to foam drainage, which occurs once the foam has blown but not completely cured. The liquid phase can drain toward the bottom of the container. Further experiments must be performed to determine if liquid drainage is the missing phenomenon that we need incorporate in order to make the model more predictive.

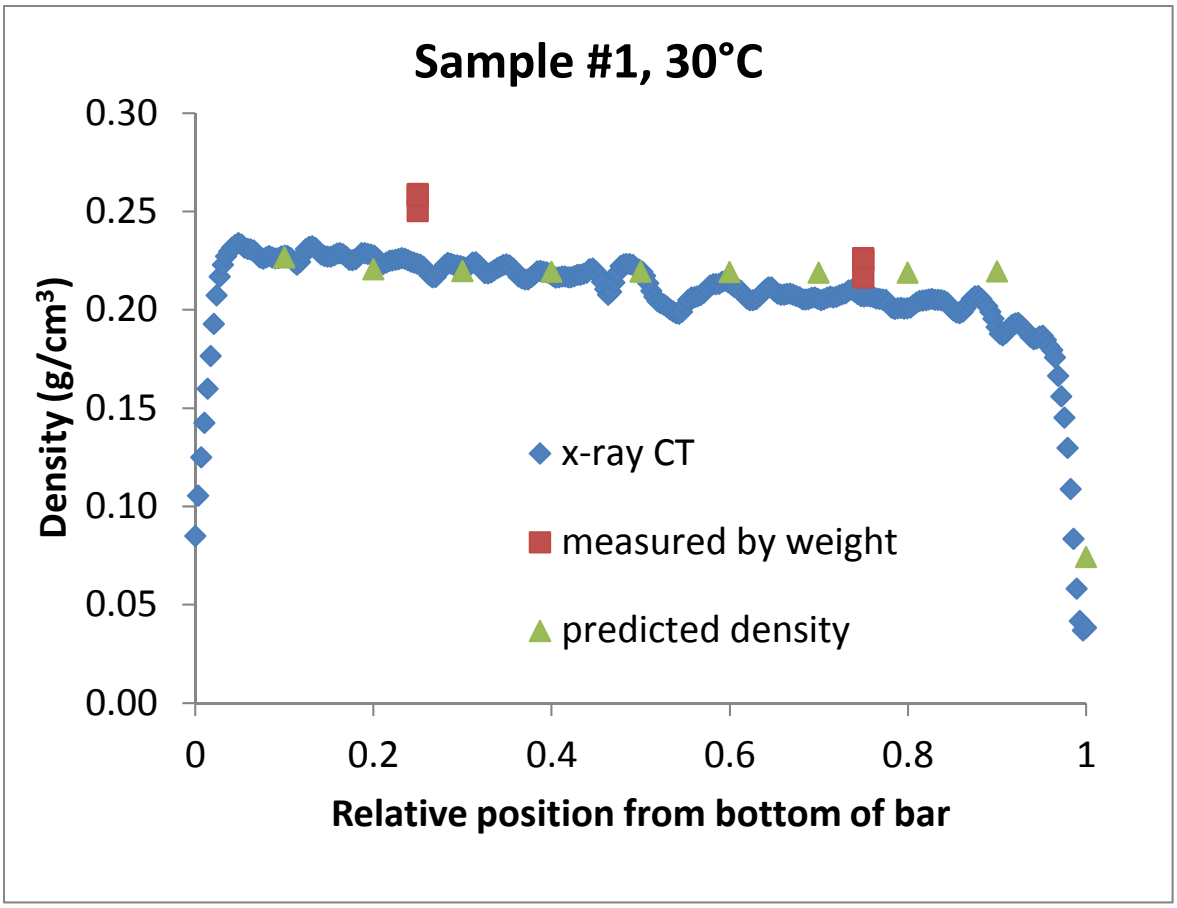

Figure 50. Comparison of density gradient from X-ray CT, weight measurement, and Sierra/Aria simulations.

Because structural foams are generally over-packed to two or more times there free-rise density, we wanted to test the model for an over-packed foam. The experiment over-packed the foam to 1.5 times its free rise density. The self-closing vents allow the air to escape but keep the foam confined to the mold, allowing it to pressurization. The amount of foam added to the mold matched the experimental amount. Results are shown in Figure 51. The predicted average density is roughly 0.325 g/cc with only small gradients.

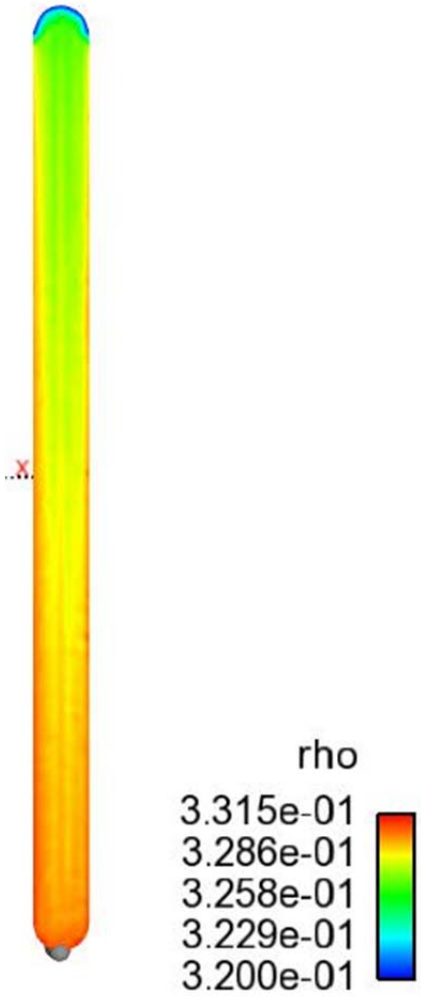

Figure 51. Density predictions from Sierra/Aria for 1.5 times over-packed foam in the bar geometry.

The density at the center of the bar from the Sierra/Aria simulation is compared to the X-ray CT density data for the over-packed foam in Figure 51. The over-packed density gradients are greater than the free-rise ones. The density predictions from Sierra/Aria show only a very small density gradient when compared to the experiment.

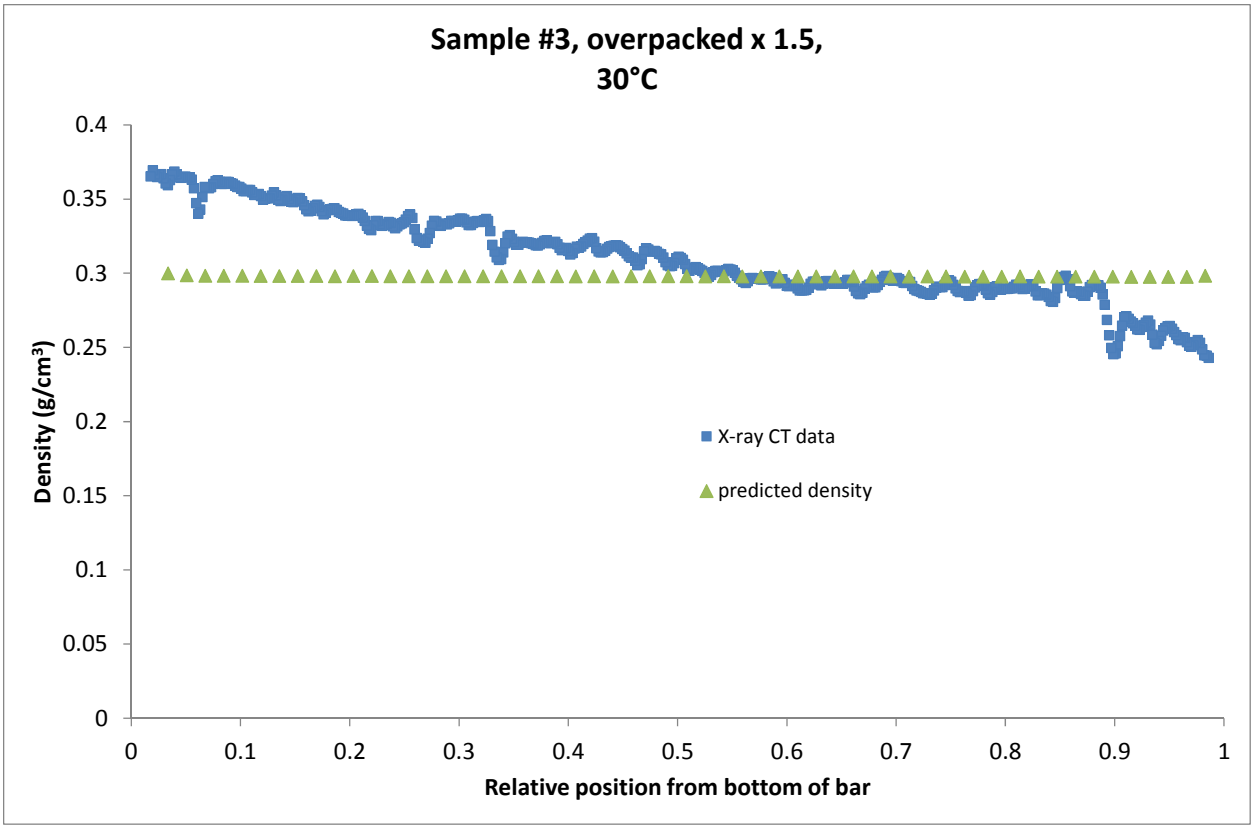

Figure 52. Comparison of density gradient from X-ray CT and Sierra/Aria predictions for over-packed foam.

6. NEXT GENERATION MODEL: LINKING BUBBLE-SCALE TO CONTINUUM FOAM MODEL

The homogenized model ignores localized effects of bubbles and bubble-scale interactions such as creaming, drainage, coalescence, coarsening, and migration away from walls. Bubble pressurization, deformation, and rupture are also important second order effects. Our current model is somewhat insensitive to viscosity. Including the viscosity in the bubble-scale size prediction will help include the viscosity time-scale that halts bubble-growth and leads to bubble pressurization. The evolving viscoelasticity that occurs between gelation and vitrification is key to slow bubble growth.

For the next generation foam model, we will need to have an estimate of bubble size so that we can include bubble-scale effects such as foam drainage, bubble-pressurization, and coarsening. To capture this phenomenon, we need to track the carbon dioxide in both the gas and liquid phases.

$$\frac{dC_{H_2O}}{dt} = -k_{H_2O} C_{H_2O}^{n}$$
$$\frac{dC_{CO_2}}{dt} = +k_{H_2O} C_{H_2O}^{n} - k_1 p_{gas} + k_2 C_{CO_2} \quad (32)$$
$$\frac{\partial}{\partial t}[\frac{4}{3}\pi R^3 \frac{p_{gas} M}{\Re T}] = k_1 p_{gas} - k_2 C_{CO_2}$$

A Rayleigh-Plesset equation is then used to determine the local bubble size over time, including both gas and liquid phase concentrations of CO_2. We propose to solve this bubble-radius equation on each element using an ordinary differential equation solver.

$$\rho(\frac{3}{2}\dot{R}^2 + R\ddot{R}) = p_{gas} - p_{liq} - 2\frac{\sigma}{R} - 4\eta_{polymer}\frac{\dot{R}}{R} \quad (33)$$

From this equation, we can see that evolving viscosity and surface tension effects will be taken into account explicitly, allowing the bubble growth to halt even if excess carbon dioxide is present. The bubble size and number will then be used to predict the density and density gradients of the macroscopic foam, including a foam drainage model linked to bubble size.

$$\phi(t) = N_{bubbles} \sum_{i=1}^{ng} \frac{4}{3}\pi R_i^3$$
$$\rho_{foam} = (\rho_{gas} - \rho_{liq})\phi(t) + \rho_{liq} \quad (34)$$

Experimental have been undertaken to determine bubble size with time for the low density encapsulation foam, Figure 53. These are optical measurements taken near a transparent wall for both a free rise and over-packed foam, so they may be slightly different than the bubble sizes and shapes seen in the bulk but we assume they will trend in a similar manner.

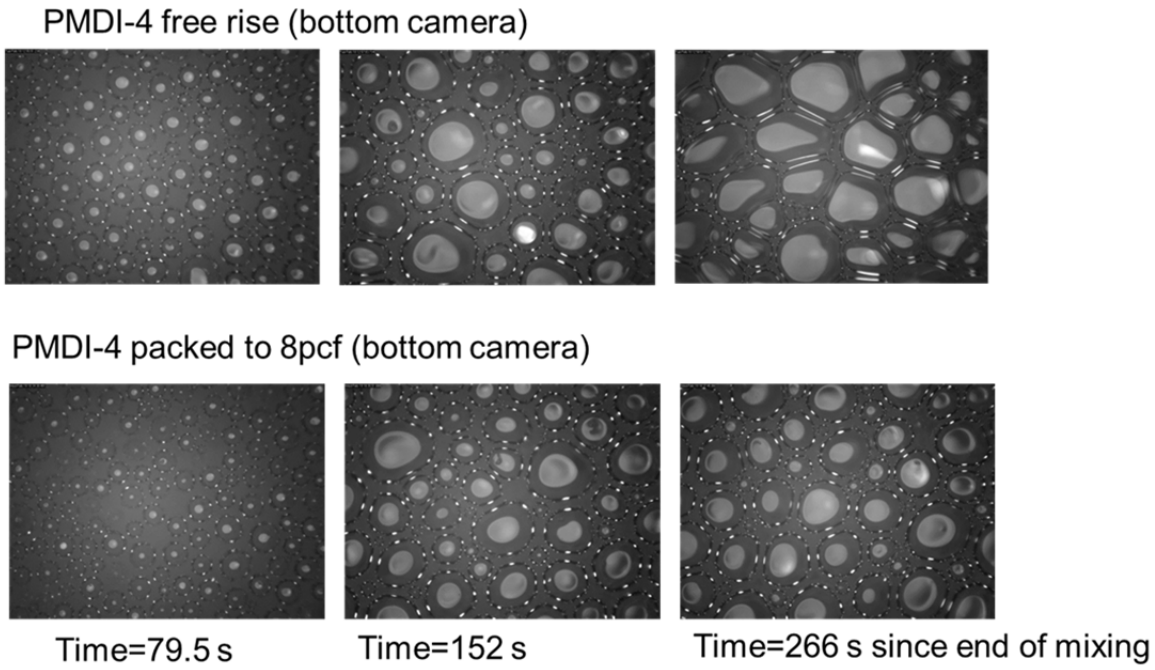

Figure 53. Optical measurements taken near a transparent wall. Here bubble shape evolves and depends on packing pressure.

From Figure 53, we can see that the over-packed foam has bubbles that stay more spherical and are less polydisperse than the free rise foam. Image processing has been used to quantify the results, Figure 54.

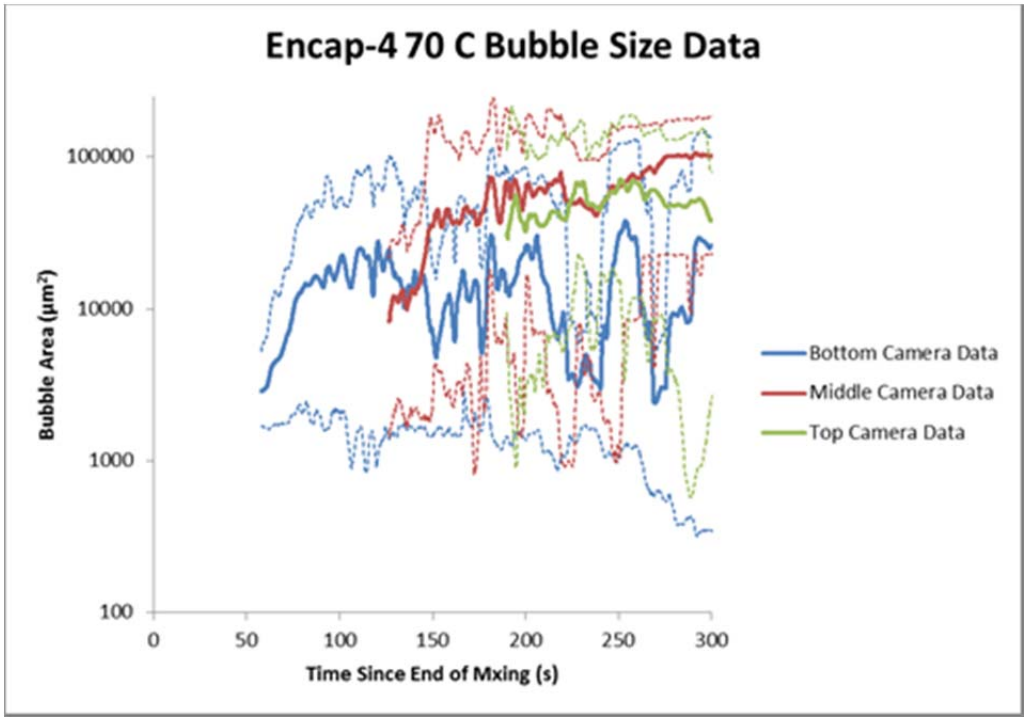

Figure 54. Bubble size as a function of time for encapsulation foam.

These results can be used to calibrate and validate the Rayleigh-Plesset equations and the density model proposed. Figure 55 shows some bubble-scale phenomena such as bubble-size polydispersity, elongation at the wall, and coarsening.

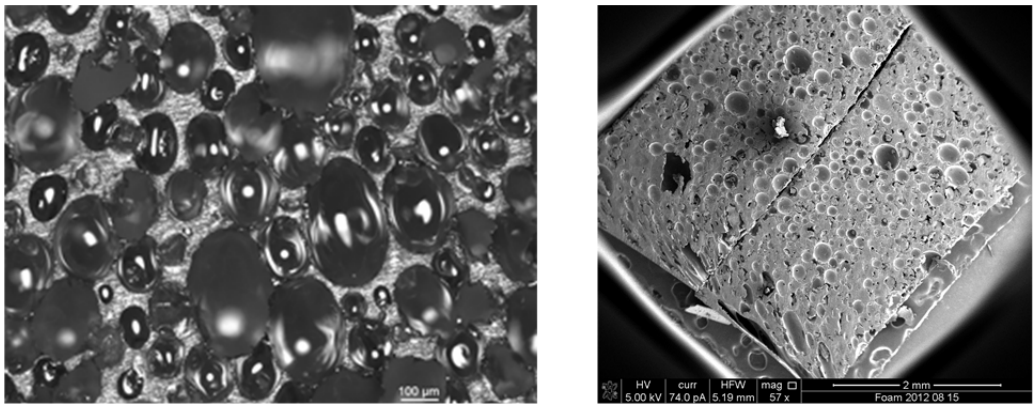

Figure 55. SEM of foam showing polydispersity (left) and bubbles at walls are elongated and show coarsening (right)

7. SUMMARY AND CONCLUSIONS

A kinetic-based numerical model has been developed for structural polyurethane, BKC 44306 PMDI-10, based on a finite element discretization and a level set method to determine the location of the free surface as the foam expands. The model includes the kinetics of polymerization via an extent of reaction equation with glass transition temperature evolution. The polymerization kinetics is fit to IR-spectroscopy data. We have developed a new kinetic approach to the gas production reaction based on the molar concentration of water, which forms carbon dioxide after reacting with isocyanate. The kinetics are fit to foam volume experiments. A viscosity model was obtained that included the effects of temperature, degree of polymerization and bubble volume fraction.

Our current model is adequate for production calculation and determining metering, initial foam placement, voids, gate, and vent locations. Our model has worked well for guiding mold design for real structural molds [Rao et al, 2015]. The model agrees qualitatively with the experimental results and gives fairly good filling profiles. A better representation of the foam and gas compressibility is important. Our current model has issues with the ideal gas representation of the gas phase, leading to numerical instabilities and negative temperatures. For future work, we need to improve the model for temperature, pressurization, and density predictions, possibly by including bubble-scale effects and an equation of state approach for the density model, with hopes that this will alleviate the numerical issues.

8. REFERENCES

D. Adolf. 1996, Measurement Techniques for Evaluating Encapsulant Thermophysical Properties During Cure, Sandia National Laboratories, SAND96-1458.

Adolf, Douglas, James E. Martin, and Jess P. Wilcoxon. "Evolution of structure and viscoelasticity in an epoxy near the sol-gel transition." Macromolecules 23.2 (1990): 527-531.

Baser, S. A., and D. V. Khakhar. "Modeling of the Dynamics of Water and R-11 blown polyurethane foam formation." *Polymer Engineering & Science* 34.8 (1994): 642-649.

Bikard, J., Bruchon, J., Coupez, T., & Vergnes, B., "Numerical prediction of the foam structure of polymeric materials by direct 3D simulation of their expansion by chemical reaction based on a multidomain method." *Journal of Materials Science* 40.22 (2005): 5875-5881.

Bikard, J., Bruchon, J., Coupez, T., & Silva, L., "Numerical simulation of 3D polyurethane expansion during manufacturing process." *Colloids and Surfaces A: Physicochemical and Engineering Aspects* 309.1 (2007): 49-63.

Bikard, J., Coupez, T., Della Valle, G., & Vergnes, B., "Simulation of bread making process using a direct 3D numerical method at microscale: analysis of baking step." *International journal of material forming* 5.1 (2012): 11-24.

Bouayad, Rabea, Jérôme Bikard, and J-F. Agassant. "Compressible flow in a plate/plate rheometer: application to the experimental determination of reactive expansion's models parameters for polyurethane foam." *International Journal of Material Forming* 2.4 (2009): 243-260.

Bird, R. B.; W. E. Stewart; E. N. Lightfoot. *Transport Phenomena*, John Wiley and Sons, New York, USA, 1960.

B. Bilyeu, W. Brostow, K. P. Menard, "Epoxy thermosets and their applications III. Kinetic equations and models," J. Mat. Ed., **23**,189-204 (2001)

Celina, Mathew, "Approximate values of CO_2 solubiltiy and diffusivity based on O_2 estimation," Personal Communication, 2013.

Dow Plastics, "Voronol 490" Form No. 109-01280 (Published 8/2001); "Papi 27" Form No. PA-26-333-0301 (Published 3/2001).

A.T. Di Benedetto, "Prediction of the glass transition temperature of polymers: a model based on the principle of corresponding states," *J. Polymer Sci., Phys.*, **25,** 1949 (1987).

Dohrmann, C. R. and P. B. Bochev, "A stabilized finite element method for the Stokes problem based on polynomial pressure projections," *Int. J. Num. Meth. Fluids*, **46**, 183–201, 2004.

Ekere, N. N.; D. He; L. Cai. IEEE Transactions on Components and Packaging Technologies 2001, **24,** 468.

Ferry J.D. *Viscoelastic Properties of Polymers 3rd Edition.* John Wiley and Sons, Inc., pp 278-279, 1980.

Geier, Stephanie, Christian Winkler, and Manfred Piesche. "Numerical simulation of mold filling processes with polyurethane foams." *Chemical Engineering & Technology* 32.9 (2009): 1438-1447.

Gibson, L. J.; M. F. Ashby. *Cellular Solids: Structure and Properties,* 2nd Edition, Cambridge Solid State Science Series, Cambridge University Press, Cambridge, UK, 1990.

Haberstroh, Edmund, and J. Zabold. "Modelling and simulation of the foam formation process." *Journal of polymer engineering* 24.1-3 (2004): 377-390.

Harran, D.; A. Laudouard. *J. Appl. Polymer Sci.* 1986, **32**, 6043.

Hilyard, N. C.; A. Cunningham, *Low Density Cellular Plastics: Physical Basis of Behavior*, Chapman & Hall, New York, USA, 1991.

T. R. J. Hughes, *The Finite Element Method*. Dover Publications, New York, USA, 2000.

Kamal, M. R., and S. Sourour. "Kinetics and thermal characterization of thermoset cure." *Polymer Engineering & Science* 13.1 (1973): 59-64.

A. M. Kraynik, T. A. Baer, M. Martinez, Sandia National Laboratories, Personal Communication, Aug. 2005.

Lefebvre, L., and Roland Keunings. "Finite element modelling of the flow of chemically reactive polymeric liquids." *International journal for numerical methods in fluids* 20.4 (1995): 319-334.

Kevin Long, Christine Roberts, Lisa Mondy, Melissa Soehnel, Hoaran Deng, Kevin Troyer, Mark Stavig, Mat Celina, Rekha Rao, "Cradle-to-Grave Modeling of Structural Foams: Nonlinear Viscoelastic Response During Manufacturing and Aging, October, 2015, SAND2015, in preparation.

Mao, D., A. D. Harvey, and J. R. Edwards. "Development of low-diffusion flux-splitting methods for gas-liquid flows with interface propagation and phase variation." *WIT TRANSACTIONS ON ENGINEERING SCIENCES* 50 (2005): 327.

Martin, J. P.; D. B. Adolf; J. P. Wilcoxon, "Viscoelasticity near the sol-gel transition," *Phys. Rev. A* 1989, **39**,1325.

Martinez, M. J.; A. M. Kraynik. "Bubble Growth during Uniform Expansion of a 2D Foam," Proc. of AIChE Annual Meeting, Nov. 1992, p. 192 (extended abstract);

May, C. A., Ed., *Epoxy Resins Chemistry and Technology*, 2nd Edition, Marcel Dekker: New York, 1988.

Modesti, M., V. Adriani, and F. Simioni. "Chemical and physical blowing agents in structural polyurethane foams: Simulation and characterization." *Polymer Engineering & Science* 40.9 (2000): 2046-2057.

L. A. Mondy; M. Celina; J. Kropka; R. R. Rao; E. Russick; N. Giron; R. Cote; J. Castaneda; J. Aubert., *Novel Foam Encapsulation Materials and Processes*, Sandia National Laboratories, SAND2010-6868, 2010.

L. A. Mondy.; R. R. Rao, M. C. Celina, A. Quintana, B. Shelden, N. B. Wyatt, E. M. Russick. Proceedings of the Polymer Processing Society 29th Annual Meeting, Nuremberg, Germany, July 15-19, 2013a.

L. A. Mondy, R.R. Rao, Bion Shelden, Melissa Soehnel, Timothy O'Hern, Anne Grillet, Mathew Celina, Nicholas Wyatt, Edward Russick, Stephen Bauer, Michael Hileman, Alexander Urquhart, Kyle Thompson, David Smith, "Experiments to Populate and Validate a Processing Model for Polyurethane Foam: BKC 44306 PMDI-10," SAND2014-3292, Sandia National Laboratories, 2014.

L. A. Mondy, A. M. Grillet; N. B. Wyatt; R. R. Rao; M. Celina; M. M. Soehnel; B. Shelden; C. C. Roberts; S. Altobelli. "Evolving Rheology of Polyurethane Foam during Expansion," presentation at the 85th Annual Meeting of the Society of Rheology, Quebec, Canada, October 13-17, 2013b.

M. Mooney, "The viscosity of a concentrated suspension of spherical particles," *J. Colloid Sci*., **6**, 162-170 (1951).

P. K. Notz; Subia, S. R.; Hopkins, M. M.; Moffat, H. K. & Noble, D. R. "ARIA Manual Aria 1.5: User's Manual," SAND2007-2734, Sandia National Laboratories, 2007.

Prud'homme, R. K.; S. A. Khan. "Experimental Results on Foam Rheology," in *Foams, Theory, Measurements and Applications*, R. K. Prud'homme and S. A. Khan (Eds.); Marcel Dekker, Inc., New York, 1996; 234.

R.R. Rao, L.A. Mondy, D.R. Noble, H.K Moffat, D.B. Adolf, P.K. Notz, Int. J. Numer. Meth. Fluids, 68, Issue 11 (2012) 1362–1392,

R. R Rao; L. A. Mondy; M. C. Celina; D. B. Adolf; J. M. Kropka; E. M. Russick. Proceedings of the Polymer Processing Society 26th Annual Meeting, Proceedings, Banff, 2010.

R. R. Rao et al., "Comparison of TL Mold Designs," Presentation to Plastics PRT, Internal Sandia presentation, March, 2015.

D. Seo; J. R. Youn; C.L.I. Tucker, "Numerical simulation of mold filling in foam reaction injection molding," *Int. J. Numer. Meth. Fluids* 2003, **42,** 1105.

L. Phinney, “Thermal Conductivity and Specific Heat Recommendations with Uncertainties for Selected Materials for B61 Thermal Analyses,” Sandia National Laboratories, OUO SAND2015-4242, May 2015.

Seo, Dongjin, and Jae Ryoun Youn. "Numerical analysis on reaction injection molding of polyurethane foam by using a finite volume method." *Polymer* 46.17 (2005): 6482-6493.

J. A. Sethian. Level Set Methods and Fast Marching Methods, volume 3 of Cambridge Monographs on Applied and Computational Mathematics. Cambridge University Press, New York, USA, 2nd edition, 1999.

Sourour, S., and M. R. Kamal. "Differential scanning calorimetry of epoxy cure: isothermal cure kinetics." *Thermochimica Acta* 14.1 (1976): 41-59.

SpecialChem, http://www.specialchem4polymers.com/tds/dabco-dc197/air-products/195/index.aspx

Taylor, G. I., “ The formation of emulsions in definable fields of flow,” *Proc. Roy. Soc. Ser. A.* **146**, 0501-0523 (1934).

R. Tesser, M. Di Serio, A. Sclafani, E. Santacesaria, “Modeling of Polyurethane Foam Formation,” *J. Appl. Polymer Sci.*, **92**, 1875, 2004.

Trilinos, http://trilinos.sandia.gov, 2015.

Williams, Malcolm L., Robert F. Landel, and John D. Ferry. "The temperature dependence of relaxation mechanisms in amorphous polymers and other glass-forming liquids," *Journal of the American Chemical society* **77,** 3701-3707 (1955).

Wilson, S. D. R., “The measurement of bulk viscosity and the elastic-viscous analogy,” *Acta Mechanica* 1997, **120**, 217.

9. DISTRIBUTION (ELECTRONIC COPIES)

1	MS0161	Legal Technology Transfer Center	11500
1	MS0346	Lisa Mondy	1516
1	MS0346	Christine Roberts	1512
1	MS0346	Anne Grillet	1512
1	MS0346	Melissa Soehnel	1512
1	MS0346	Kevin Troyer	1526
1	MS0382	Shayna Begay	2153
1	MS0382	Kyle Zufelt	2153
1	MS0382	Heather Boldt	2153
1	MS0386	Jeff Lantz	2159
1	MS0555	Kyle Thompson	1522
1	MS0828	Tracie Durbin	1512
1	MS0828	Paul Crozier	1541
1	MS0828	Basil Hassan	1510
1	MS0836	Rekha Rao	1516
1	MS0836	David Noble	1516
1	MS0836	Tony Geller	1516
1	MS0840	Kevin Long	1554
1	MS0840	Daniel Rader	1513
1	MS0840	Jim Redmond	1550
1	MS0878	Amy Kaczmarowski	2735
1	MS0888	Edward Russick	1833

1	MS0888	James McElhanon	1835
1	MS0958	Nicholas Wyatt	1835
1	MS9042	Amanda Dodd	8253
1	MS9042	Victor Brunini	8253
1	MS9403	LeRoy Whinnery	8223
1	MS1411	Mat Celina	1819
1	MS0899	Technical Library	9536

External:
James Tinsley, Jim Mahoney, Angela Kartsonis
NNSA's National Security Campus, Operated by Honeywell Federal Manufacturing & Technologies, LLC, D/891 Advanced Engineering Simulations & Analysis, Kansas City, Mo.


Sandia National Laboratories